CONF-9505285--1

LA-UR- 3018

Title: HIGH BRIGHTNESS BEAMS AND APPLICATIONS

Author(s): R. L. Sheffield

Submitted to: Workshop/Development & Applications of Free Electron Lasers
Beijing, China
May 29 - June 6, 1995

MASTER

Los Alamos
NATIONAL LABORATORY

Form No. 836 R5
ST 2629 10/91

HIGH BRIGHTNESS BEAMS AND APPLICATIONS

RICHARD L. SHEFFIELD
Los Alamos National Laboratory, MS H851, Los Alamos, NM 87544 *

Abstract This paper describes the present research on attaining intense bright electron beams. Thermionic systems are briefly covered. Recent and past results from the photoinjector programs are given. The performance advantages and difficulties presently faced by researchers using photoinjectors is discussed. The progress that has been made in photocathode materials, both in lifetime and quantum efficiency, is covered. Finally, a discussion of emittance measurements of photoinjector systems and how the mesurement is complicated by the non-thermal nature of the electron beam is presented.

* Work supported by Los Alamos National Laboratory Directed Research and Development under the auspices of the United States Department of Energy.

1. INTRODUCTION

This series of talks covers the generation of high-brightness electron beams and the associated accelerator structures. Our work on high-brightness accelerators was motivated by the need to directly produce high quality electron beams. Damping rings can be used to produce high brightness beams, but cost and complexity inhibit wide deployment of damping ring technology. Also some of the electron beam applications require few-picosecond long pulses, shorter than can be produced with damping rings.

Several accelerator applications require high-charge, high-quality electron beams. Free-electron lasers (FELs) are widely tunable, high-power sources of light capable of generating wavelengths not accessible to conventional laser systems. The design of many FELs requires high peak currents and high brightness beams for high gain. Another application is

the reduction in cost or elimination of damping rings. A reduction in cost is possible because a brighter electron is used for injection into the ring. With a brighter beam the ring acceptance can be reduced with a consequent reduction in cost. One other application is Compton scattering. For efficient Compton scattering the electron beam must be focused into a small volume again necessitating a high-brightness beam.

A brief outline of this paper follows. After a general introduction to basic electron physics, we will compare different approaches to the generation of electron beams. For very high-brightness high-charge electron beams, the photoinjector appears to be the appropriate electron source. Following the discussion of electron sources, a description of the overall design of a high-brightness accelerator is presented. The high-brightness accelerator uses a technique of emittance reduction called emittance compensation This is followed by a review of an accelerator system, named the Advanced Free-Electron Laser (AFEL), based on the preceding design work. The AFEL section will cover design, construction, operational characteristics, and experimental results. The subsequent section covers the measurement of emittance using the quadrupole scan technique. Although the quad scan is a commonly used technique for measuring emittance, in a photoinjector-based system this technique can lead to erroneous emittance measurements. Finally a few of the possible applications of an AFEL system are presented.

2. PHASE SPACE AND EMITTANCE

To understand the performance of an electron machine, we need to quantify the quality of the electron beam. This quantification is done using the concepts of phase space and emittance.

Phase space is the basic tool by which charged particle beam transport is characterized. Phase space is typically represented by a two-dimensional plot of x' versus x, where x is the transverse rms radius and x' is the particle's angle with respect to the optic axis,

$$x' = dx/dz = (\gamma m dx/dt)/(\gamma m dz/dt) = p_x/p_z, \qquad (2.1)$$

where m is the electron mass, and γ is the relativistic gamma, p_x is the transverse momentum and p_z is the forward momentum.

Plots of the phase space of a zero transverse-temperature and zero energy-spread beam are schematically represented in the left figure of Figure 1(a). The optical-ray trace equivalent to those ray-trace plots is schematically shown in the right figure of Figure 1(a). As can be seen in the phase space plots in Figure 1(a), a line with a negative slope represents a converging beam, a vertical line represents the beam at a focus, and a horizontal line represents a beam with a focus at infinity.

Beams and the beamline optics are not perfect. As a consequence, beams cannot be focused to infinitely small spots (uncertainty principle aside). Figure 1(b), (c), (d), and (e) gives a few of many effects that can impact the focusability of an optical beam. An electron beam would have analogous effects in either its phase space or it's equivalent optics. The spot size of a beam as measured with a diagnostic is the projection of the beam distribution on the x-axis. The beam at its focus is defined to have the smallest extent along the x-axis.

For thermalized beams, as shown in Figure 2, or a distribution that does not have recoverable correlations in phase space, a good measure of the focusability of a beam is the rms emittance of the beam.[1] The rms normalized emittance, ε_n, is calculated from the rms emittance, ε_x. The emittances are calculated using the equations,

$$\varepsilon_n = \beta\gamma\varepsilon_x = \pi\beta\gamma(\langle x^2\rangle\langle x'^2\rangle - \langle x \cdot x'\rangle^2)^{1/2}, \qquad (2.2)$$

where β is the particle velocity divided by the speed of light and x and x' are the particle's transverse coordinate and angle of divergence from the optic axis, respectively, and <> means an average over the electron distribution f(x,y,z):

$$\langle x^2\rangle = \frac{\int\int\int f(x,y,z)\, x^2\, dx\, dy\, dz}{\int\int\int f(x,y,z)\, dx\, dy\, dz} \; . \qquad (2.3)$$

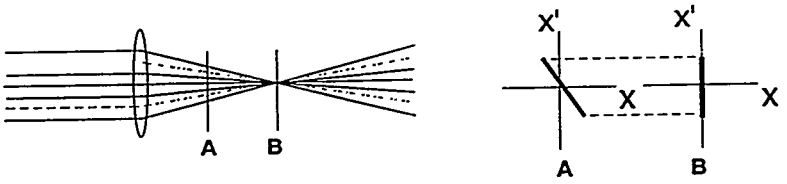

Figure 1(a)

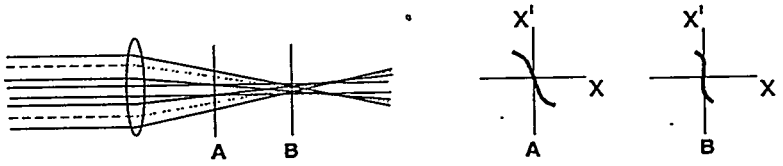

Figure 1(b)

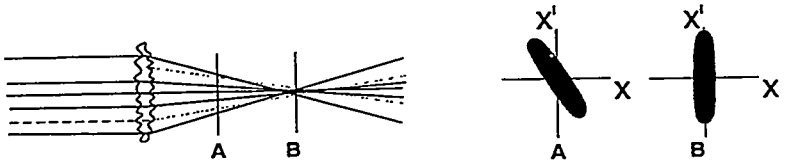

Figure 1(c)

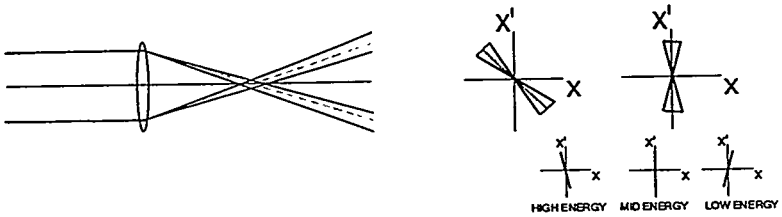

Figure 1(d)

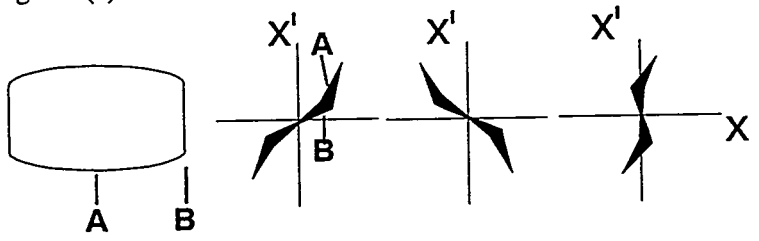

Figure 1(e)

Figure 1. In the left plot in (a), a collinear optical beam impinges on a perfect optic, passes through position A and is focused at position B. In the right plot in (a), the phase space plots corresponding to the two locations of A and B are given. In (b), the focusing optic has an incorrect curvature. In (c), the focusing optic's surface is rough. In (d), a beam composed of three energies (or wavelengths in the case of light) is focused. In (e), the first phase plot is a drifting beam expanding under the influence of space charge. The longitudinal middle of the beam at position A has more charge than at position B. The beam goes through a lens in the second phase plot in (e), and the third phase plot is the beam at a focus after the lens.

Beam dynamics are determined by transport of the phase space ellipse using matrix representations of the beamline optics. Either of two approaches are used to described the beam ellipse, the Twiss parameter or sigma matrix representation.[2] Figure 3 is a schematic showing the relationship between the Twiss and sigma matrix parameters.

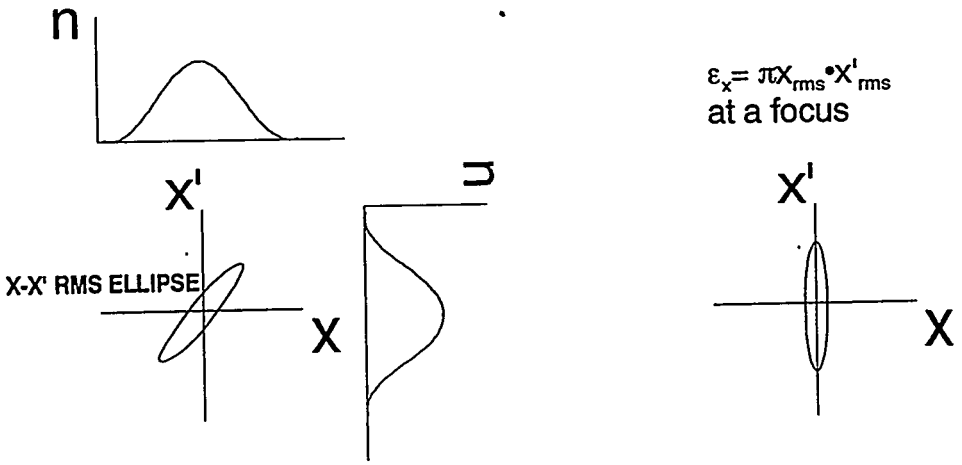

Figure 2. The area of an ellipse calculated from the rms x and rms x' values equal the rms emittance, ε_x, of a beam. This area is easily calculated at the beam's focus.

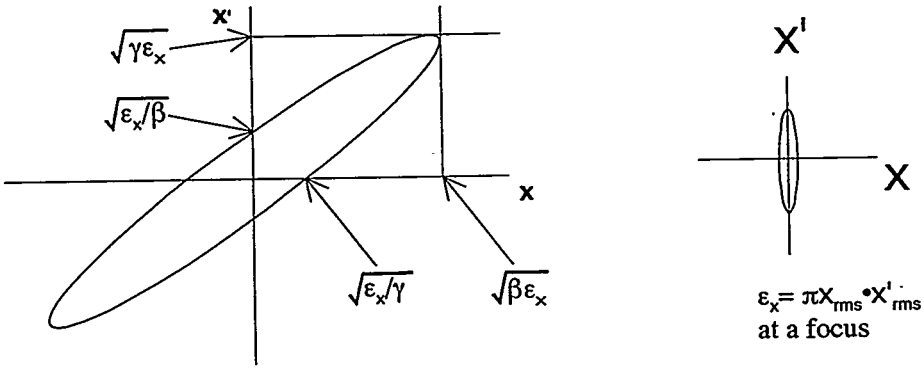

Eq. for using Twiss parameters: $\gamma x^2 + 2\alpha xx' + \beta x'^2 = \varepsilon_x$, $\beta\gamma - \alpha^2 = 1$

Eq. for using sigma parameters: $\sigma_{22}x^2 - 2\sigma_{21}xx' + \sigma_{11}x'^2 = \varepsilon_x^2$, $\sigma_{22}\sigma_{11} - \sigma_{12}^2 = \varepsilon_x^2$ where $\sigma_{22} = \varepsilon_x\gamma$, $\sigma_{11} = \varepsilon_x\beta$, and $\sigma_{12} = \sigma_{21} = -\varepsilon_x\alpha$.

Figure 3. Description of the Twiss parameters and sigma matrix parameters used for beam transport simulations. Note that β and γ are not the relativistic parameters.

Louiville's theorem states that the 6 dimensional phase space density is invariant.[3] However, because of the manner in which most experimental diagnostics work and the techniques that the computer simulations use to calculate emittance, only a projection of the phase space ellipse onto x-x' (or y-y' or r-r') plane is calculated. An emittance calculated from a projection of phase onto a plane is not a conserved quantity. This impacts the emittance experiments described later in this paper.

3. ELECTRON SOURCES

3.1 Thermionic Sources

To have a high-brightness electron beam, either the electron gun system must directly produce a bright beam or a damping ring must be used. Electron guns using a long pulse or a dc beam rely on a well-designed gun producing a beam that has a beam temperature near the thermal limit of the electron source. The beamline design after the gun depends on if the application ultimately requires a dc beam or a short pulse. For a dc beam (or pulsed beams where the pulse end effects are negligible), very good quality beams can be produced if care is taken in the beam transport design. If the application requires a short pulse, then a bunching system must be designed that preserves the beam quality throughout the bunching and acceleration process. Preserving beam quality is difficult because of the effects of nonlinear rf fields in the bunching cavities and the space-charge forces present at subrelativistic energies.

3.1.1 DC guns

DC guns can be produce beams with an emittance near the thermal limit determined by the cathode. The lower limit of the beam's normalized emittance from a thermionic electron source is governed by the emitter size and by the transverse component of the thermal motion of the electrons. The thermal limit of the normalized rms emittance of a beam from a thermionic emitter of radius r_c at a uniform absolute temperature T is

$$\varepsilon_n = 0.5\pi r_c(kT/m_oc^2)^{1/2} \quad \text{[units: m} \cdot \text{rad]} \tag{3.1}$$

because $\langle x \cdot x' \rangle = 0$ at the cathode.[4] For a typical thermionic emitter at 1160 K, the average transverse energy of emitted electrons is 0.1 eV. For a uniform current density J, the total current is $I = \pi r_c^2 J$ and the lower limit on the rms emittance is

$$\varepsilon_n = 1.25 \times 10^{-6} (I/J)^{1/2} \ \pi \cdot \text{mm} \cdot \text{mrad}, \qquad (3.2)$$

with J in A/cm^2.

The current density from a dispenser cathode is typically not more than 20 A/cm^2; for example, the lowest achievable rms emittance for 1 cm^2 thermionic cathode is 0.28 π mm-mrad.

The following information on very long pulse (>> 1 ns) and dc injectors is a summary of a paper[5] by W. Herrmannsfeldt. These types of guns are well suited for two applications: first, for electron cooling of ion beams and, second, for electrostatic free electron lasers (FEL). The design of a DC gun must include the effects of space charge. Figure 4 is a schematic of a DC gun designed for the University of California at Santa Barbara.[5] In the gun, the space-charge self-force in the beam is canceled out with a carefully designed focusing electrode at the Pierce angle,[6] thus maintaining a uniform current density. Also, the exit energy of the beam from the gun should be as high as possible to minimize further space charge defocusing downstream from the gun. If the beam maintains a uniform profile up to relativistic energies, then the beam emittance can be near the cathode-limited thermal temperature.

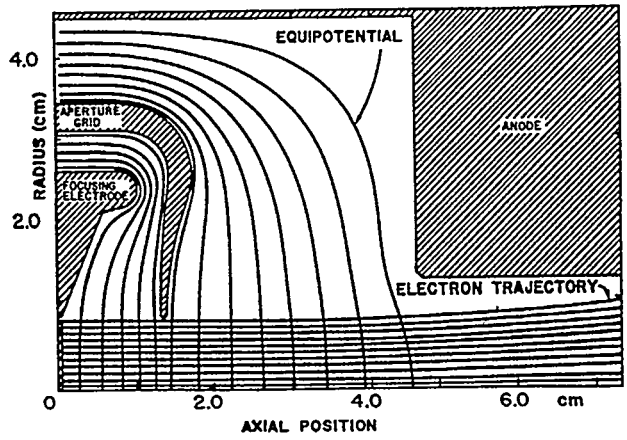

Figure 4. DC gun designed for UCSB.

Unfortunately, many applications require high charge per bunch in short pulses. The process by which the beam is processed for acceptance into rf accelerator structures causes the emittance to grow by at least an order of magnitude. Also, high repetition rates (>1 MHz) are difficult. As stated above, bunches can be accelerated with a dc field and not suffer the emittance growth that is due to time-varying effects typically found in rf accelerators. The addition of harmonics to the rf accelerating fields has been proposed to eliminate this source of emittance growth. A design[7,8] that corrects for the time-varying fields in a radio-frequency (rf) accelerator uses cavities that operate at the third harmonic of the main linac frequency. Two conditions must be met to approximate a dc accelerating field during pulse transit. First, the amplitude of the third harmonic is set to nine times the fundamental frequency's amplitude. Second, the phase of the third harmonic is chosen to decelerate the bunch at the peak acceleration of the fundamental. The amplitude can be made flat to within 0.1% over 37° of the rf. However, the resulting two-frequency cavity will have increased phase and amplitude control complexity.

For relativistic beams, the harmonic component may be added with separate cavities, considerably reducing cavity design and control complexity. Improved accelerator performance using separated cavities for the first and third harmonic has been verified using PARMELA by Todd Smith.[7] After initial acceleration to several MeV with a long pulse (to minimize space-charge effects), the peak current is then increased using magnetic compression. The design is given in Table 1.

3.1.2 RF guns

The construction of the Mark III accelerator has been described in detail elsewhere.[9] The layout of the experiment is shown in Figure 5. The machine parameters are as follows: macropulse length of 2 to 5 μs, micropulse length of 2.2 ps, gun energy of 1 MeV, and a magnetic compression of 10 from the alpha magnet. The alpha magnet is also a momentum filter and limits the electron energy spread to less than 0.5%.

The electron source in the Mark III is a LaB_6 cathode. The cathode produces electrons by thermal emission. However, because the electrons are emitted at all phases of the rf, many of the electrons are accelerated at the wrong phases for matching into the main linac. The electrons accelerated at the wrong phases degrades the cathode because of the electron back bombardment. The peak current was 33 A. The gun x by y emittance was approximately 2 by 4 π mm-mrad, respectively.

Table 1 Injector designed by T. Smith for the Stanford High-Energy Physics Laboratory's Superconducting Accelerator[7]. Calculated emittance using PARMELA is 5 π·mm·mrad. The blocks indicate the beamline structure, and under each block are the beam energy, pulse length, and peak current.

300 keV ELECTRON SOURCE	HARMONIC BUNCHER	HARMONIC ACCELER-ATOR	MAGNETIC BUNCHER
300 keV	300 keV	2.5 MeV	2.5 MeV
333 ps	100 ps	100 ps	5 ps
3 A	10 A	10 A	200 A

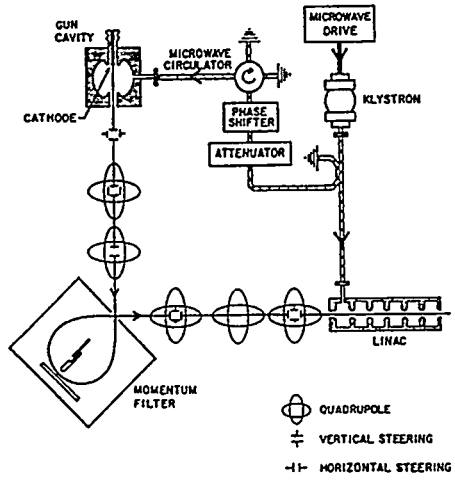

Figure 5. Schematic of the experiment showing microwave feed system and the path of the electrons from the laser-switched thermionic gun to the Mark III accelerator.

3.2 Photocathodes

Photoemitters can produce very high charge densities. For example, Cs_3Sb photoemitters have effective temperature of 0.2 eV or greater.[10] The electron thermal temperature is not simply the difference between the incident photon energy and the semiconductor band gap (a difference of 0.7 eV for Cs_3Sb) because of phonon scattering in the semiconductor crystal lattice. This cathode is capable of delivering[19] over 600 A/cm^2, giving a minimum emittance of 0.07 π mm-mrad for a 1 cm^2 cathode. However, the brightness of the source normally does not limit the final brightness of the beam. Instead, the acceleration process and transport through a beamline can increase the beam emittance by over an order of

magnitude. A design that effectively utilizes photocathodes is called a photoinjector and is described in Section 4.

Photocathodes can be divided into two classes based on quantum efficiency (QE): low QE and high QE. Low QE cathodes are characterized by having reduced vacuum requirements and are relatively easy to produce. The low QE cathodes fall into two groups, metals and thermionic emitters.

3.2.1 Low quantum efficiency

Many different metals have been considered for photoinjector cathodes. Copper and magnesium[11] are the most common choices. Other metals that have been considered are: Al, Au, stainless steel, Sm, Y, W, Zn, Au, Mo, Ta, Pd, Zr, Ba, Na, and Ca.[12,13,14] Measurements of quantum efficiency vary considerably among individual researchers. This variation can in part be attributed to differences in samples, preparation techniques, and contamination before and during measurements. Also the UCLA group has reported non-uniform emission occurring after use in a photoinjector.[15] Overall, the measured quantum efficiency of metals varies from less than 10^{-8} to 3×10^{-3} near a wavelength of 250 nm.

The thermionic emitters, LaB_6[16] and BaO, have also been used as cathodes, both heated and unheated. Again, the measured quantum efficiencies are dependent on many factors and varies among laboratories. Quantum efficiencies of greater than 10^{-4} have been measured. The temporal response in the picosecond regime for these cathodes has not been measured.

Another metal cathode being used in the ATF at the Kharkov Institute is a pressed pellet of BaNi. They quote a QE of 1.7×10^{-3}.[17]

3.2.2 High quantum efficiency

High QE photocathodes usually require a good vacuum and have a more sophisticated fabrication procedure. These types of cathodes can be subdivided into three categories: multialkali, crystal-like, and GaAs.

The Cs_3Sb multialkali cathode was the first cathode used in a photoinjector. Since then, a large number of other multialkali cathodes have been used, such as CsK_2Sb, AgO:Cs, CsNaKSb, K_3Sb, and NaK_2Sb.

Multialkali cathodes have a significant advantage over metal cathodes. These cathodes have QE's over 2% at 532 nm, making the drive laser requirements less stringent. Unfortunately, since they rely on a cesium barrier to reduce the surface work function to near zero, they tend to be very susceptible to contamination and require 10^{-10} torr vacuum

systems. Because of contamination issues, these cathodes have limited lifetimes.

The crystal-like cathodes, Cs_2Te, CsI, K_2Te all require laser wavelengths of at least 250 nm for quantum efficiencies over 2%. Their advantage is that they can survive in 10^{-8} vacuum systems.[18,19] Also these cathodes can be rejuvenated by heated to 150 C and reused.

Finally, GaAs has been used for many years as a polarized electron source. KEK plans to use this cathode in a specially cleaned photoinjector that exhibits almost no change in impurities and background pressure with and without rf power. [20]

There is a wide variety of photocathodes to choose from based on the system requirements. The photocathode, though difficult, is no longer a major impediment to using this technology.

4. PHOTOINJECTORS

A schematic of a photoinjector is shown Figure 6. From the first use of a photoinjector in 1985,[21] many different systems have been designed to meet the needs of very different applications. The applications include high-average-current electron beams, high-brightness sources for free-electron lasers and colliders, high pulse charges for wakefield accelerators, high-duty factor picosecond high-energy x-ray pulses, and picosecond soft x-rays by Compton scattering. The advantage of this source for Compton scattering is that the drive laser for the photocathode can be used as the scattering laser. Using the drive laser provides sub-picosecond synchronization of the electron pulse and the laser pulse.

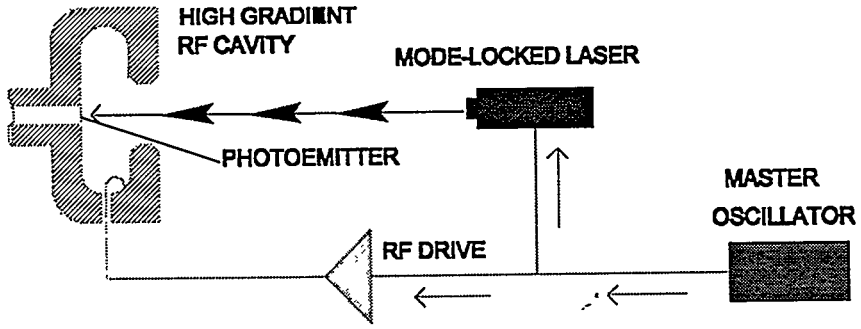

Figure 6. Basic components of a photoinjector are a laser, a photocathode, an rf source, and an rf cavity

Photoinjectors[21] have several unique characteristics. A high gradient rf cavity is used to supply the accelerating field. The high-gradient not only reduces space charge effects, but the gradient also enables laminar flow from the cathode through the accelerator to the beamline. Since the electron beam does not undergo transverse or axial mixing, a large fraction of the emittance growth due to space charge can be corrected by a technique called emittance compensation,[22] described in Section 4.6. The high gradient also allows the extraction of high charge for closely spaced pulses enabling the production of high-average currents.[23]

Since the electron source is a photocathode illuminated with a laser, the machine designer has complete control over the spatial and temporal characteristics of the electron emission process. Figure 7 is a demonstration of the spatial control of the electron beam by placing a mask in the laser beam that illuminates the cathode. Also, the gun can directly produce very short electron pulses limited only by the gun gradient and charge in the pulse. For instance, 1 nC from a cathode with a surface gradient of 30 MV/m will have a 6 ps pulse length.

4.1 First Photoinjector Experiment

The motivation for the first photoinjector experiment Figure 8, was the need for an electron source that has an rms emittance of less than 10 π mm-mrad and the capability of generating greater than 1 A average current. The ability of a photoinjector to demonstrate that level of performance was demonstrated in this first experiment (Figure 9).

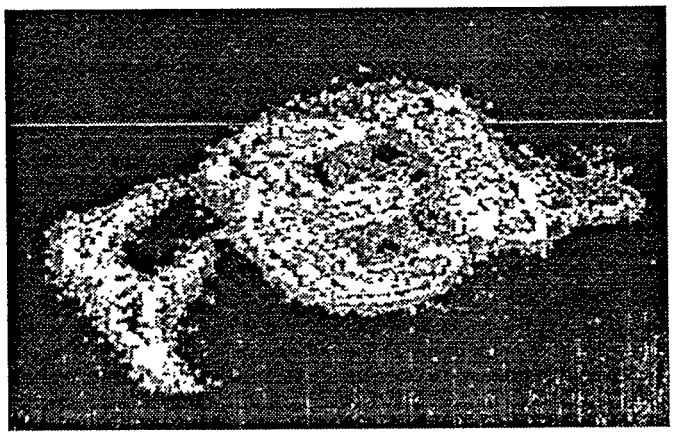

Figure 7. Electron beam image taken by a camera viewing an optical transition radiation screen 7 meters downstream of the cathode. The electron beam energy was 17 MeV. The photocathode was illuminated by a laser with a mask placed in the beam. The letters "FEL" were cut into the mask.

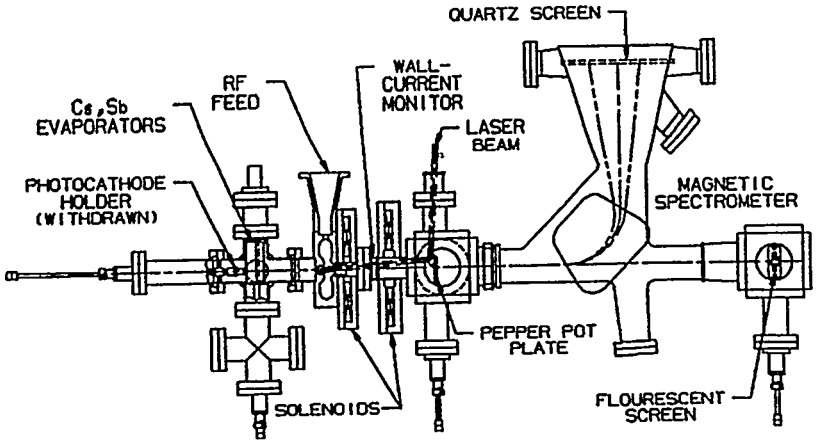

Figure 8. The first photoinjector experiment demonstrated an emittance of less than 8 π mm-mrad at 10 nC, a maximum 27 nC per 53 ps long micropulse, and 2.9 A average current for a 6 μs long macropulse. The current density was estimated to be 600 A/cm^2 from a Cs_3Sb cathode.

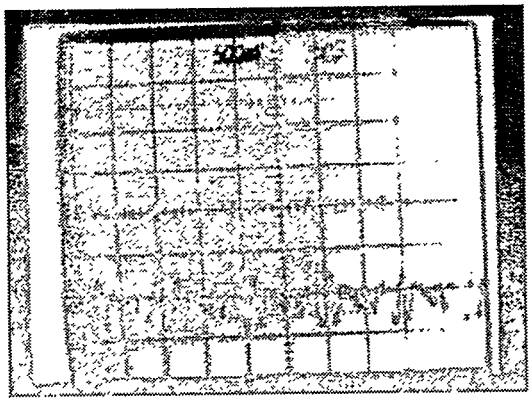

Figure 9. The first photoinjector experiment generated 2.9 A average current for 10 μs at 1 MeV, with peak micropulse currents of 390 A and micropulse charge of 27 nC. The horizontal scale is 5 ns/div. The vertical scale is 13 nC/div.

4.1.1 Experimental Design

The photocathodes for that experiment were fabricated in a preparation chamber vacuum coupled to the rf linac. Following fabrication in the preparation chamber, the photocathode is inserted into the rf cavity.

When the quantum efficiency of the photocathode decreases below some arbitrary minimum value, the substrate was pulled back and heat cleaned at 400°C. A new photocathode was then fabricated over the existing substrate without opening the UHV system.

The photocathode was illuminated with a frequency-doubled Nd:YAG laser. The laser is mode locked at 108.33 MHz, the twelfth subharmonic of 1300 MHz. The mode-locking crystal is driven by the same master oscillator that drives the 1300-MHz rf klystron and is phase locked to the rf. The laser generated 100-ps pulses at 1.06 μm that, after frequency doubling to 532 nm, become 70-ps-long pulses. The power available at 532 nm is approximately an average of 250 kW over 10 μs.

4.1.2 Experimental Measurements of Emittance

The experimental parameters for the emittance measurements were 11 nC (200-A peak), 70-ps Gaussian temporal width, less than 0.4-cm beam radius at the cathode (was not accurately measured at the time of the experiment and only the upper bound is known), 1.0-MeV beam energy, and a solenoid field of 1.8 kg. The measured emittance was 10 π mm-mrad. The measured emittance did not agree with a PIC simulation (which gave greater than 35 π mm-mrad) of the experiment. This disagreement led to a detailed examination of the gun, beamline, and the pepper-pot emittance diagnostic using PARMELA and MASK[24] simulations.

The experimental and simulated electron-beam diameter at the pepper pot and the diameters of the beamlets produced by the pepper pot at the second quartz screen are in close agreement, confirming the accuracy of the simulations. The emittance of the electron beam for that experiment, with 10 nC per bunch, was calculated from the simulations to be 30 π mm-mrad for 100% of the beam. Simulations[24] show that, if the beam is clipped in time and left with 80% of the original charge, then the emittance of the remaining beam was calculated to be 10 π mm-mrad in agreement with the experimental results. The results of the MASK calculations are shown in Figure 10.

Although neglecting the temporal tails of the distribution consequently gives low emittance, most applications of bright electron beams depend upon only the bright central core of the electron bunch. More importantly, the accuracy of the simulation codes was verified for the future linac design.

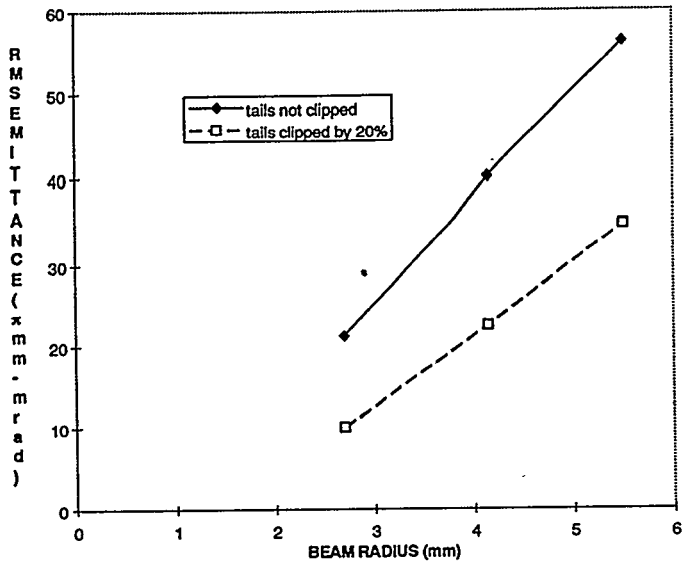

Figure 10. The beam emittances from MASK simulations (performed by Bill Herrmannsfeldt of SLAC) are within the experimental error in beam radius if the temporal tails of the Gaussian pulse are not included. The two curves show the difference in emittance gained by excluding a small fraction of the charge at the front and tail of the pulse.

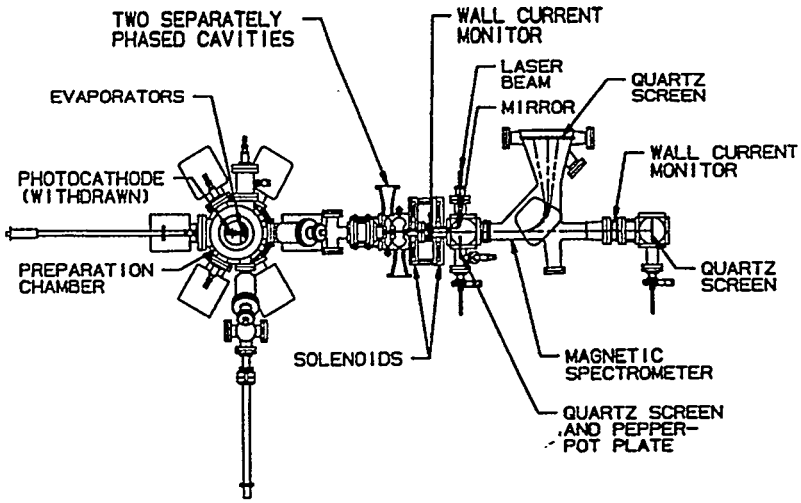

Figure 11. Two-cavity experiment showing gun, beam transport, and diagnostics.

4.2 Second Photoinjector Experiment

A second experiment using two-cavities, shown Figure 11, followed the single cavity experiment. The linac had two 1300-MHz rf cavities with independent amplitude and phase controls. Both rf cavities had loops to measure the phases and amplitudes of the rf fields present in the cavities. Following the second cell were the diagnostics for bunch charge, beam energy, emittance, and temporal profile. The details of the rf cavity design are presented elsewhere.[25]

The electron energy gain for typical operation was 0.9 MeV in the first cavity and 1.8 MeV in the second cavity. This corresponds to operating both cavities at approximately 2 Kilpatrick (58 MeV/m peak surface field).

The above mentioned laser for the single cavity experiment was modified for the two-cavity experiment. A Spectra-Physics pulse compressor was added to the optical train for generation of 4- to 20-ps pulses. The laser pulse length was limited by the gain bandwidth of the Nd:YAG amplifiers to approximately 16 ps. The maximum charge extracted for this pulse was 13.2 nC from 1 cm^2 of photocathode surface. This gives 820 A/cm^2 of current density at the cathode. However, PARMELA simulations predict that a 16-ps electron pulse increases to 22 ps on passage through the first cavity, giving a peak current after the first cavity of 600 A.

4.3 Mark III Photoinjector

The microwave rf gun for the Mark III accelerator was also run in a photoinjector mode. The current emission from the cathode was limited by average-power heating; therefore, by using a laser to limit the emission to the correct rf phase, higher peak currents can be obtained.[26] Also, the lifetime of the cathode is expected to be longer. In this mode, the LaB_6 cathode was operated just below its normal emission temperature, and a laser was used to pulse the cathode. Operation with the laser resulted in an increase in peak current from 33 A to 75 A with no observable loss in beam emittance.

4.4 Photoinjector Lasers

The key to the stability of a photoinjector is the drive laser. The advantage of using a laser is that the cathode can be illuminated with any temporal and spatial profile required to optimize the gun performance. Lasers have excellent temporal stability, with almost all of the present systems in use having less than picosecond temporal jitter. Also, if only single pulses are

required, a laser can generate very large energy per pulse (LLNL NOVA laser can generate nearly 1 kJ in less than 10 ns).

The remaining difficulty in the laser systems is the macropulse to macropulse amplitude stability. Achieving less than 10% amplitude stability is very difficult with present systems. The technology exists to achieve less than 1% stability, but not the resources. Present laser stability measurements[27] are less than 0.5 ps and less than 1% amplitude variations.

Lasers can generate high peak energy in short pulses easier than long (many microseconds) pulses. It follows that for long pulse trains a minimum QE of 0.5% is required.

One other issue that can be critical to stable operation is pointing stability. Since the laser defines the spatial profile of the emission, the laser must be stably pointed at the cathode. For example, the large solenoid around the gun region of the Advanced Free-Electron Laser[28] acts to amplify small transverse spatial variations of the cathode position. This amplification occurs because of the long distance from the large solenoid to the first focusing element (2.5 m lever arm). Even though the cathode diameter is 8 mm, a shift of 100 microns in the centroid will image to a 25 micron shift in the middle of the wiggler significantly degrading the performance of an FEL.

4.5 Present Photoinjector Designs

Photoinjectors routinely generate greater than 500 A/cm^2. For most systems this current density is limited only by the field gradient on the cathode or the laser intensity.

Research is still proceeding on high-average current machines at Boeing Defense and Space,[29] and at Bruyeres-le-Chatel.[30] The first demonstration of a high-average current using a photoinjector was on the Boeing accelerator. This 25% duty factor machine has demonstrated an average current of 32 mA at 5 MeV, giving an average beam power of 160 kW. The macropulse average current was 0.13 A. The beam emittance was 5 to 10 π mm-mrad for 1 to 7 nC pulse charge. An example of the machine located at Bruyeres-le-Chatel is shown in Figure 12.

Many designs are based on the work done at Brookhaven National Laboratory at 2856 MHz.[31] A schematic of one of their guns is shown in Figure 13. The Brookhaven type of gun is being used for advanced accelerator studies, free-electron lasers, and linear collider injectors. One of the advantages of operating near 3 GHz is the higher cathode surface electric fields that can be obtained relative to operating at lower frequencies.

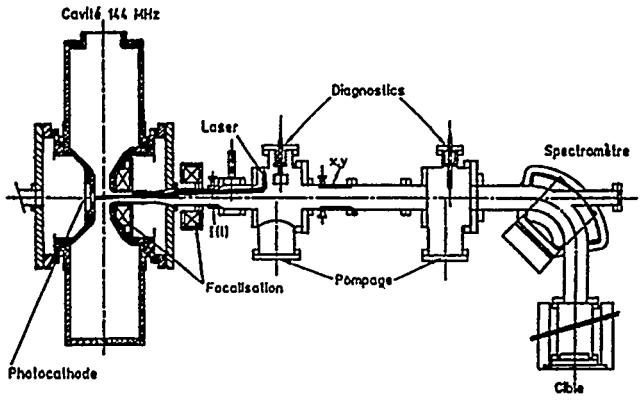

Figure 12. Photoinjector at LEL-HF Bruyeres-le-Chatel. RF cell produces a 2.0 MeV beam at 5 nC with a pulse length of 20 to 50 ps. They have measured 4 π mm-mrad at 1 nC.

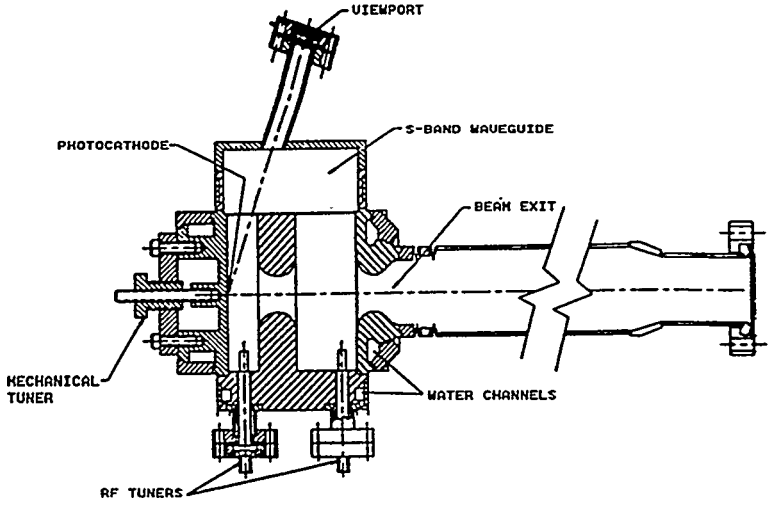

Figure 13. Brookhaven's 2856 MHz photoinjector operates at 3 MeV and has produced 4 π mm-mrad at 1 nC with a cathode field of 70 MV/m. The gun has generated 4.5 MeV beams. This photoinjector uses two cells operating in a π-mode configuration with a single radio-frequency feed. Copper or magnesium is typically used for the cathode.

A new photoinjector operating at 17 GHz has been constructed at the Massachusetts Institute of Technology (MIT). This gun has 1-1/2 cells with peak surface fields of 250 MV/m and a peak cathode surface field of 200 MV/m. The rf source is a gyro-amplifier developed at MIT. [32]

Photoinjectors have generated micropulse charges between 1 and 30 nC. However, Argonne National Laboratory has generated greater than 60 nC per micropulse.[33]

Electron pulse lengths are limited by space charge effects in the first few centimeters in front of the cathode. Typically, less than 10 ps pulses is generated for 1 nC of charge in a micropulse (in the AFEL 6 ps for 1 nC)

The measured electron beam's rms emittance varies, depending on the machine design, between 1 and 5 π mm-mrad for 1 nC in a micropulse. Some newer designs give less than 1 π mm-mrad for 1 nC by scrapping the wings of the distributions.[34]

4.6 Emittance Compensation

Emittance compensation[35] is a technique for decreasing the growth in emittance that occurs in a low-energy charged particle beam with large space charge forces. The technique uses a focusing element (a solenoid or quadrupole) to correct for the distortions in phase space that occurs when a beam expands due to the space charge forces. A representative configuration is shown in Figure 14.

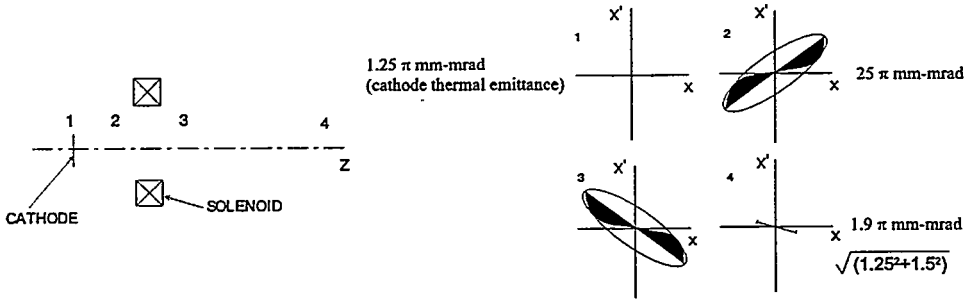

Figure 14. At the cathode, the electron bunch emittance is determined by the cathode's thermal emittance (position 1). As an electron bunch leaves the cathode, the bunch expands radially due to radial space charge forces. Since the space charge force acts continuously on the bunch, no single discrete lens can compensate for the distortion of the distribution in phase space (position 2). However, if a simple lens can be used to focus the bunch (position 3), then, the same types of forces that acted on the bunch during expansion are present while the bunch is focused (position 4). The figure also shows the residual emittance (1.5 π mm-mrad) after emittance compensation is used.. A thermal emittance of 1.25 π mm-mrad is the cathode emission temperature of Cs_3Sb.

A fully non-linear model for emittance compensation cannot be solved analytically. However, simplified models can be solved. To demonstrate the basic principles, our model has the following assumptions. A beam with linear radial electric fields. The beam has non-relativistic velocities perpendicular to propagation. The beam's radius does not change significantly and therefore the force is approximately a constant with respect to the radius and time. The beam's longitudinal velocity is approximately the speed of light. With these assumptions the radial electric field, $E(r,\zeta,t)$, is

$$E(r,\zeta,t) = -m*k(\zeta)*\rho/e \text{ and } F= m*d^2r/dt^2 = -e*E = m*k(\zeta)*\rho, \quad (4.1)$$

where m is the electron mass, $k(\zeta)$ is the force constant that can vary with longitudinal position, ζ is the relative longitudinal coordinate, ρ is the relative radial position, and e is the electron charge. Figure 15 shows the relationship between the relative and absolute coordinates.

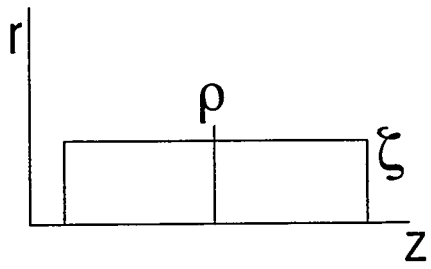

Figure 15. A plot of the relative coordinates ρ and ζ with respect to radius, r, and longitudinal position, z.

The radial force, $F(r,\zeta,t)$, is

$$F(r,\zeta,t) = m*d^2r/dt^2 = -e* E(\rho,\zeta,t) = m*k(\zeta)*\rho \quad (4.2)$$

Then the radius is

$$r = k(\zeta)*\rho*(t-t_0)^2/2+dr/dt_{(t=t_0)}*(t-t_0) + r_0, \quad (4.3)$$

and the radial velocity is

$$dr/dt = k(\zeta)*\rho*(t - t_0) + dr/dt_{(t=t_0)}. \quad (4.4)$$

Setting $z = c*t$, $dr/dt = (dr/dz)*(dz/dt) = r'*c$ and $r'_0 = dr/dt_{(t=0)}/c$, then

$$r = k(\zeta)\bullet\rho\bullet(z-z_0)^2/2/c^2 + r'_0\bullet(z-z_0) + r_0, \; r' = k(\zeta)\bullet\rho\bullet(z-z_0)/c^2 + r'_0. \quad (4.5)$$

In phase space a useful relationship is the ratio between r and r'. The closer this ratio is to a constant, the straighter the line in phase space and the lower the emittance. Solving for the ratio gives

$$r'/r = [k(\zeta)\bullet\rho\bullet(z-z_0)/c^2 + r'_0]/[k(\zeta)\bullet\rho\bullet(z-z_0)^2/2/c^2 + r'_0\bullet(z-z_0) + r_0]. \quad (4.6)$$

Assuming the initial conditions $z_0 = 0$, $r = r_0$ and $r'_0 = 0$, then

$$r'/r = [k(\zeta)\bullet z/c^2]/[k(\zeta)\bullet z^2/2/c^2 + r_0/\rho] \sim k(\zeta)\bullet z/[c^2 \bullet r_0/\rho], \quad (4.7)$$

therefore r'/r is approximately proportional to ρ. This gives a curved line in phase space for each location ζ as shown in Figure 16. By focusing this beam with a simple linear lens with a focal length, f, of

$$f = (z_d - z_l)^2/(2z_d) \quad (4.8)$$

and located at position z_l, it is possible to fully compensate at position z_d for the curvature in phase space.

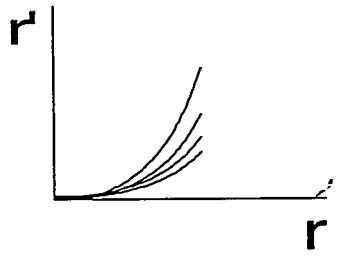

Figure 16. Phase space in r versus r' for a beam that has expanded under a linear space charge force. Each curved line represents a differing force constant $k(\zeta)$.

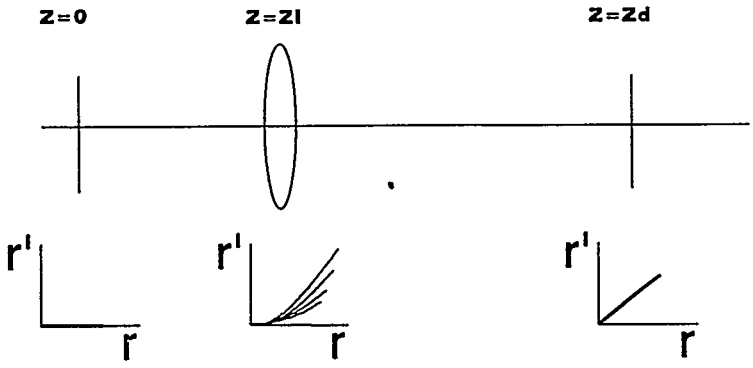

Figure 17. Plots of a beam with different space charge forces in longitudinal slices being focused with a lens at position z_l. At position z_d the beam slices overlap and are straight lines, giving a zero emittance beam.

The ratio of r/r' is then

$$r'/r = 2z_d/(z_d^2-z_l^2). \qquad (4.9)$$

Since r'/r is independent of k(ζ) and ρ, we get a superposition of straight lines in phase space for all k(ζ), as shown in Figure 17.

The effect of space charge on a finite length pulse for larger variations in radius is not analytically soluble. However, the same focusing technique can correct for emittance growth. A first order expansion of the equations was solved exactly by Carlsten.[35]

5. ADVANCED FREE-ELECTRON LASER

A new accelerator design that produces a very bright electron beam in a compact form has been developed through the Advanced Free-Electron Laser Initiative[36] (AFELI) at Los Alamos National Laboratory. The goal of AFELI was to build a second-generation free-electron laser (FEL). This FEL was designed to be suitable for a wide range of industrial, medical, and research applications. State-of-the-art components were incorporated so that the FEL system is compact, robust, and user friendly.

The accelerator design incorporates the experience gained from the initial photoinjector experiments described earlier in his paper and the later accelerator experiments at APEX (APLE Prototype EXperiment).[37]

The design simulations were performed using a modified version of the code PARMELA.

The emittance is calculated in two ways. The "full" emittance is calculated by using the entire micropulse in time and space. The "slice" emittance is calculated by dividing a micropulse into slices in time equal to a slippage length. To ensure enough particles are in a slice to give reasonable statistics, the smallest time slice is limited to 1% of the total pulse length. We calculate the slice emittance because the electrons do not generate gain over the entire pulse, but only for the middle portion (in time) of the pulse. The individual slices can have different divergence's, and so the only a few of the slices may be properly matched and not the entire pulse. If temporal mixing occurs, the use of slice emittance is invalid and the full rms emittance must be used. To minimize mixing and to preserve beam brightness, great care must be given to proper beam-line design.[38]

5.1 Accelerator Construction

The design goals for the AFEL accelerator are to maximize beam brightness, develop a simple design, and operate at the relatively high duty factor of 0.1%. The design point is greater than 2 nC charge per micropulse and an effective emittance of less than 10 π mm-mrad. Simple design is accomplished by using a single radio-frequency feed to drive the entire accelerator structure. The $\pi/2$ mode, 10-1/2 cell accelerator (Figure 18) has the following features: 20-MeV output energy, average cavity gradients of 22 MeV/m, 10-Hz repetition rate, 20-μs long macropulses, 8- to 20-ps long electron micropulses, and liquid-nitrogen capable operation. The accelerator operates with a 1300-MHz, 15-MW-peak-power klystron.

At 15 MeV, the peak rf power lost to copper is 5 MW. The beam power is 7.5 MW for 0.5 A average current corresponding to 4.6 nC per micropulse at 108 MHz or 2.3 nC at 216 MHz. Assuming 20% control margin (2.5 MW above 12.5 MW), 50% of the rf power is converted into beam. Although the rf macropulse is 18 μs long, to avoid cavity transients, the electrons are turned on during the last 15 μs of the rf pulse when the cavity field is flat.

5.1.1 Using a Solenoid to Compensate for Emittance Growth Caused by Space Charge

The use of a solenoid to reduce emittance growth caused by space charge was discussed in Section 4.6. Thus, proper lens placement can significant reduce the emittance growth. A unique solenoid design follows from the

requirements of minimum emittance growth and simultaneously having the beam focused at a particular axial location. The solenoid design depends on the accelerator gradient, current density, and location of the peak magnetic field with respect to the cathode. A schematic of the AFEL accelerator's magnetic fields is shown in Figure 19. The emittance numbers in Figure 14 are from a typical PARMELA run. To accurately render the solenoid field profiles, we incorporated the POISSON field maps of the solenoid directly into PARMELA.

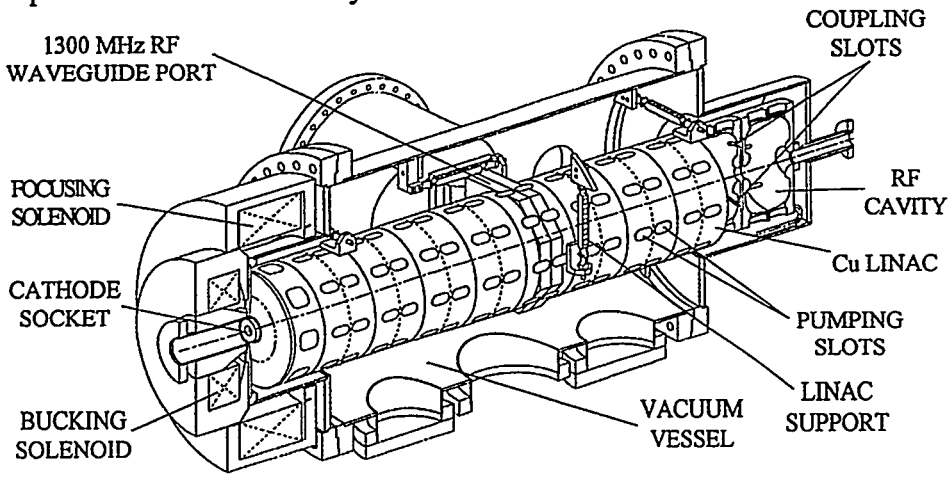

Figure 18. AFEL linac schematic.

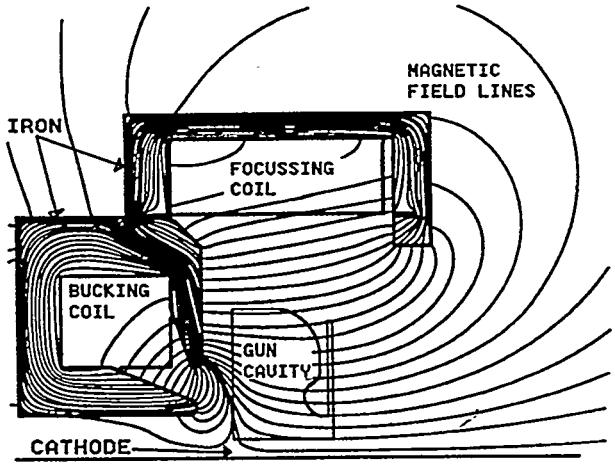

Figure 19. The AFEL linac design must have proper lens placement to minimize emittance growth.

From simulations, we computed the effect on the final emittance caused from the cathode thermal effects. As expected, the final emittance is the sum of squares of the final emittance calculated with zero cathode temperature and the finite cathode emittance. An example is shown in Figure 14.

5.1.2 Minimizing Perturbations caused by Accelerator Coupling Slots

The APEX accelerator[37] was the first more than two-cell-photoinjector design. The standing-wave, 1300-MHz, π-mode accelerator is designed with on-axis coupling slots. The initial PARMELA simulations gave a symmetrical beam at the accelerator exit (Figure 20). In the APEX experiment, however, the accelerator produced elliptical beams. By incorporating MAFIA field maps of the coupling slots into PARMELA, we found that the coupling slots produced a quadrupole lens in every accelerator cell. A sample output plot of the APEX photoinjector from the modified PARMELA is shown in Figure 21.

Several possible configurations of on-axis coupling are shown in Figure 22. A single slot produces a dipole lens, two slots produce a quadrupole lens, four slots produces an octupole lens, and so on. Each accelerator cell (except the cells at the accelerator ends) has coupling slots on each half an accelerator cell. The two-coupling-slot configuration gives a quadrupole lens at the entrance and exit of the accelerator cell. The orientation of the slots will determine whether the quadrupole lenses add or subtract focusing for each cell. In the APEX arrangement (type H) the fields at each cell end are additive, giving a net quadrupole lens. In a type T arrangement the fields at each cell end cancel, giving a net effect close to zero.

The cancellation of the quadrupole effects in a type T arrangement is nearly zero only for a highly relativistic beam. In the first few cells, where the beam is still not highly relativistic, a net quadrupole lens still exists. Also, the large solenoid around the gun cell causes the beam to rotate azimuthially. If a quadrupole field overlaps the solenoid field, the x and y phase spaces will mix, causing an irrecoverable growth in emittance.

The coupling-slot design for the AFEL accelerator uses a four-coupling-slot arrangement for the first two cells and a type T configuration for the remaining accelerator cells. Because the four-slot arrangement has no quadrupole component, the first two cells produce no beam asymmetry. After the beam exits the first two cells, the beam is highly relativistic and the type T coupling gives a very small net quadrupole focusing. This configuration is shown in Figure 23.

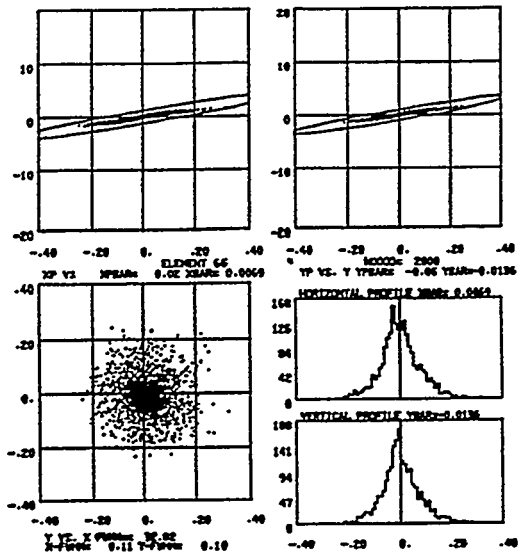

Figure 20. PARMELA simulation result neglecting the effects of coupling fields. The upper left picture is the x' versus x phase space, the upper right is the y' versus y phase space, the lower left is the beam spot plotted as y versus x, and the lower are the horizontal and vertical profiles. X and y are in centimeters, and x' and y' are in milliradians.

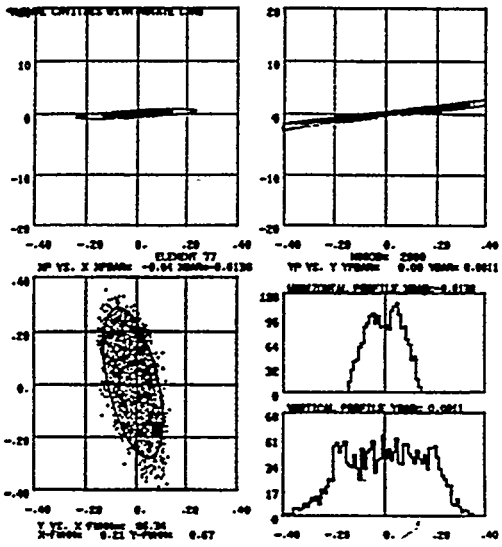

Figure 21. PARMELA simulation result with the type H coupling-cell configuration.

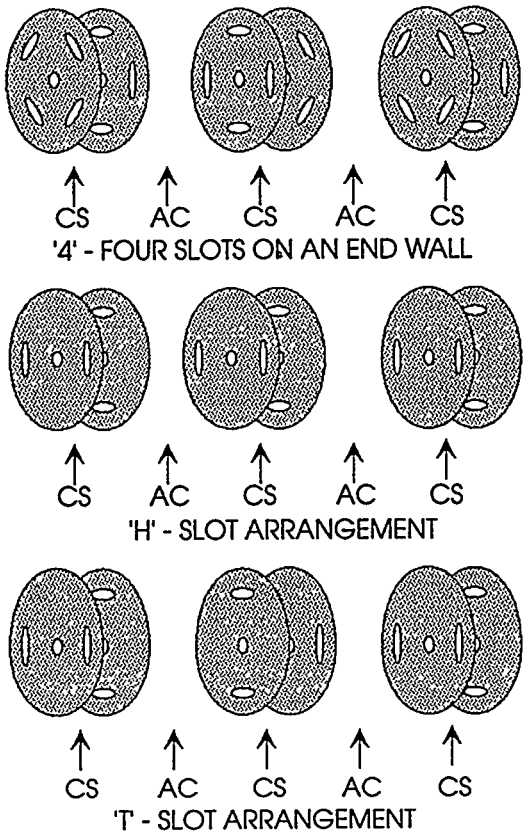

Figure 22. Possible coupling-slot arrangements with four- and two-slot coupling. CS is a coupling cell. AC is an accelerator cell.

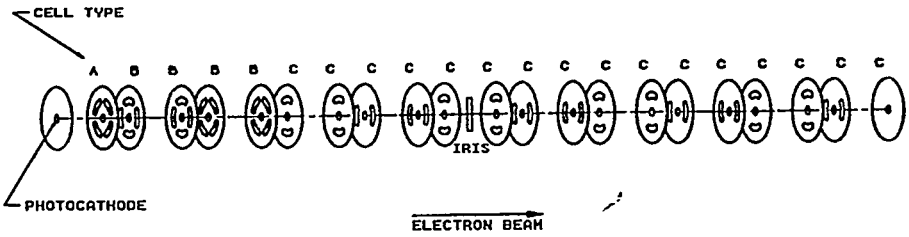

Figure 23. Schematic of the AFEL's coupling slots and accelerator cells. The A, B, and C above the cells indicate different cavity shapes.

The four-coupling-slot arrangement cannot be carried throughout the accelerator. At the high-average currents of the AFEL, beam breakup will occur because of the coupling of a dipole mode from cell to cell. In the type T- and H-coupling-cell configuration, the dipole mode does not couple because the coupling slots are rotated 90^{o} in the coupling cavity. In the 4-slot coupling-cells, the slots are rotated 45^{o} in the coupling cavity, which very effectively couples the dipole modes.

The PARMELA simulation for the coupling slot arrangements shown in Figure 23 is presented in Figure 24.

5.1.3 Other Features of the AFEL Accelerator

The first cell, a half-cell, is 9 mm longer than one-half of a standard 1300-Mhz cell. A longer injection cell has two advantages. First, the exit phase of the electron bunch depends on the cell length. Since the AFEL linac has a single rf feed, the proper operating phase to minimize energy spread was met by adjusting the first cell length. Second, a longer first cell increases the electron-beam energy at the exit of the first cell. This reduces the space-charge effects and helps improve the final emittance. The exit energy from the first cell is 1.5 MeV instead of 1.0 MeV for a regular half-cell.

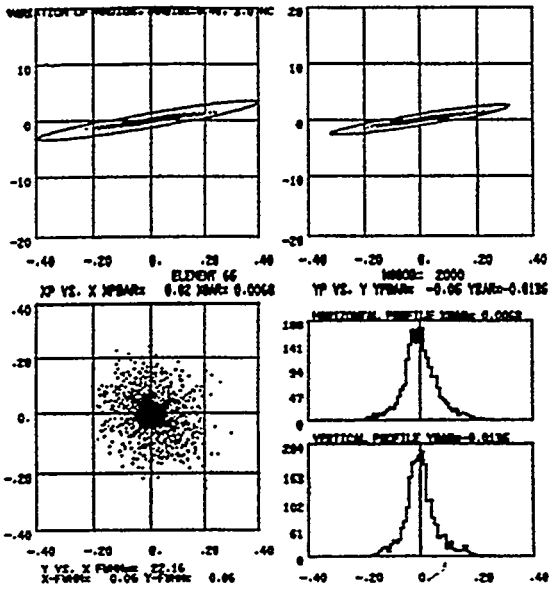

Figure 24. PARMELA simulation result for the AFEL accelerator, including all of the coupling slot effects..

Other engineering features of the AFEL accelerator are the capability of operation at 77K; UHV design; and high-Q, high-gradient accelerator cells.

5.1.4 Beam Dependencies

This type of accelerator is unique in that the electron-beam distribution does not mix longitudinally. With no mixing, the rms emittance calculation for the full pulse underestimates the FEL performance. Figure 25 shows the x- and y-slice emittance during a micropulse for a Gaussian and a square pulse. Except for statistical noise caused by the limited number of particles in the simulation, the slice emittance is time independent during the micropulse. However, the emittance of the full pulse is significantly larger. The larger full-pulse emittance is caused from the variation in divergence throughout the micropulse (see upper graph in Figure 26). Two factors help determine FEL performance: first, the local beam conditions in the micropulse (since the slippage length is a small fraction of the entire pulse length); second, the ability to match into the gain profile of the wiggler. Figure 26 shows the beam conditions that affect FEL performance. The upper two graphs are the beam divergence and the particle density as a function of time. The lower graph is a calculation of $\Delta\nu$[39] (gain width for a sample wiggler) as a function of time. The three graphs show that most of the electrons are in the gain width of the wiggler for the middle portion of a micropulse. The beginning and end of the micropulse are not matched into the wiggler, but the fraction of the electrons in the temporal wings is small. Again, this type of analysis is not correct if the beam mixes longitudinally.

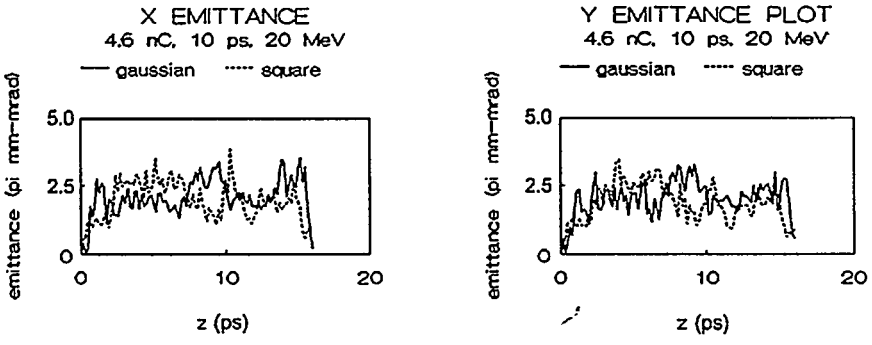

Figure 25. Plots of the slice emittance during a micropulse. The plots give results for pulses that are either Gaussian or square in time. The bottom graph compares the 90% emittance and the middle of the pulse emittance.

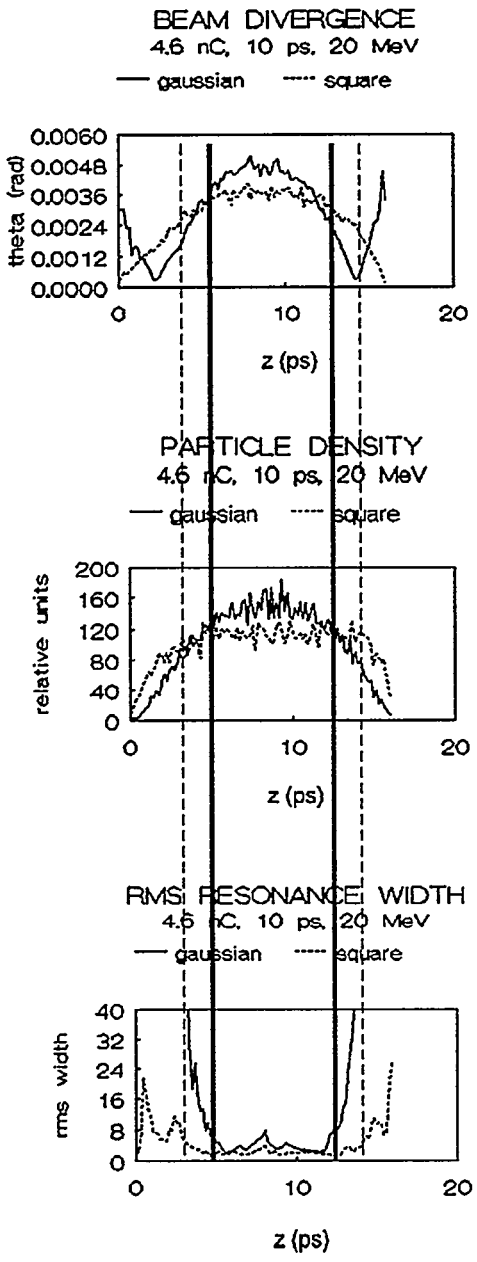

Figure 26. The upper plot shows the beam divergence during the pulse. The middle plot shows the charge density during the pulse. The bottom plot shows how well matched the pulse is to the gain profile of the wiggler. The solid (dotted) lines through all three plots represent the fraction of a Gaussian (square) beam that is well matched to the AFEL wiggler.

The AFEL is designed to minimize components and distances and to increase reliability and ease of use. However, the performance of the FEL design does depend strongly on a few parameters. The parameters that must be tightly controlled are: the radius of the cathode, the magnitude of the solenoid field around the cathode region, the centering of the cathode relative to the center of the magnetic field, the accelerator phase, and the magnitude of the accelerator fields.

5.1.5 Engineering Issues

The accelerator is typically run between 13 to 19 MeV. At a beam energy of 18 MeV, the first cell gradient is 23 MV/m and the remaining accelerator cells' gradients are 20 MV/m.

Field emission from the cathode depends on the surface properties and gradient present in the cathode cell. Designs of high-duty-factor machines or experiments where the background charge levels are important must include the effect of the field emission. The field emission can occur either directly from or near the photocathode. Thus the maximum cell gradient might be limited, impacting the beam emittance. High-QE cathodes seem to exhibit more field emission than the low-QE cathodes. The surface of the cathode can also impact the field emission. Cathodes in which the machining grooves can be seen exhibit much high field emission than cathodes given a mirror polish.

The spatial profile of the photocathode laser and photocathode QE is important. In general, spatial profiles in which the electron density decreases with radius, as opposed to radially uniform or slightly increasing with radius, produce a greater emittance.

To preserve a bright electron beam throughout the beam-line requires detailed simulations. The AFEL beam line was designed[4] and the parametric sensitivities measured[40] using PARMELA.

5.2 Laser and Photocathode

The photoinjector front-end consists of a drive laser and a Cs_2Te photocathode. The drive laser starts with a Nd:YLF oscillator mode-locked at 108.33 MHz (12th subharmonic of the accelerator frequency). A transverse Pockel cell switches out variable-length, programmable macropulses to be amplified in a double-pass amplifier. Frequency doubling in a lithium triborate crystal converts 50% of the 1.05 μm infrared light to 527-nm green light. Following the doubling crystal is quadrupling crystal, generating 263 nm light. A typical 15-μs macropulse consists of 1,600 micropulses, each approximately 10 ps long. Space charge effects increase the electron pulse width depending on the beam

energy and the charge density. For 15-MeV beams, an illuminated area of 0.4 cm^2 and a micropulse charge of 3 nC, the calculated electron pulse width is 15 ps.

The photocathodes exhibit a typical quantum efficiency (QE) of 10% after they are fabricated. Due to poisoning during the transfer process, their QE is reduced to 5% in the linac. A typical cathode's useful lifetime has not been systematically measured. To extend beam time and provide flexibility in trying new cathode materials, the photocathodes are prepared six at a time (a "6-pack") in a separate preparation chamber. The 6-pack is then transported under vacuum to the accelerator via an actuator/inserter mechanism. The time required between preparation of new six-packs is greater than a month.

5.3 Beamline Construction

The Advanced FEL, Figure 27, with a 1-cm-period wiggler has been in operation since early 1993 in the spectral region between 4.5 and 6 μm, limited by the bandwidth of multilayer dielectric optics.[41] With metal mirrors, the Advanced FEL can be tuned from 4 to 12 μm. A broader tuning range (3 to 20 μm) can be achieved by lasing at fundamental and harmonic frequencies with a high-field, 2-cm-period wiggler.

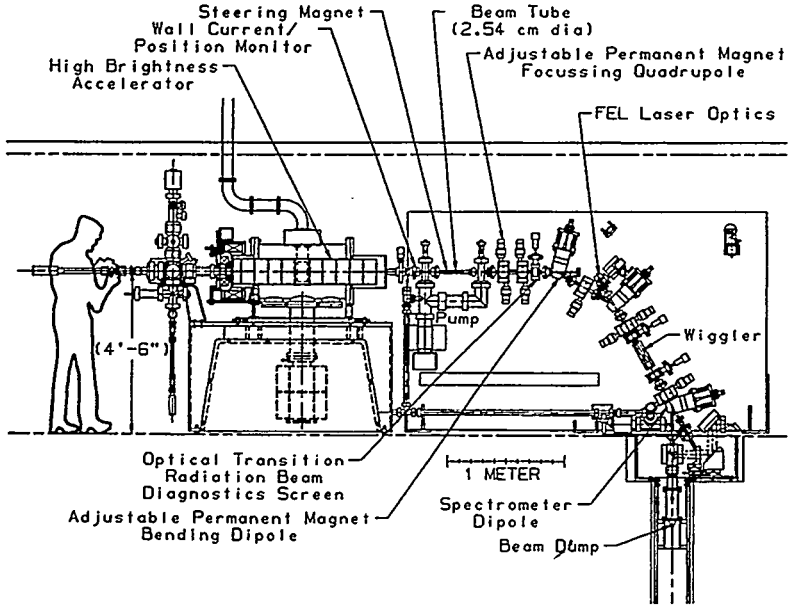

Figure 27. Layout of the AFEL beamline showing cathode insertion mechanism, accelerator, electron optics, and FEL optics.

5.3.1 Electron Beam-line

The beam-line consists of three 30-degree bends. The first bend allows direct visual access to the cathode. Thus the drive laser beam is line-of sight with the cathode. The second bend deflects the electron beam into the FEL optical axis. The third bend deflects the beam into an electron energy spectrometer. The electron beam then goes into a carbon-block beam-dump. The first two bends are made achromatic by a single quadrupole that refocuses the beam in the dispersion plane. The beam is matched into the two bends by setting the first two quadrupole doublets so that the beam is focused in x-plane (the bend plane) in the center of the dipoles and in y-plane at the quadrupole singlet. For compactness and reliability, all focusing quadrupoles and bending dipoles are made out of permanent magnets. Detailed designs of the variable-field permanent magnet quadrupoles and dipoles have been reported.[42] The use of permanent magnet components offers two advantages: a) once the electron beam is aligned through the wiggler, lasing can be reproduced every day with only minor adjustments of the beam optics, and b) the permanent magnet optics do not need power or cooling, thus simplifying the design.

To transport the beam through the beamline around the bends and through a 2.8-mm-id wiggler tube, we relied on TRACE 3D to set the quadrupoles to approximately the correct values. The beam profiles were then measured using optical transition radiation (OTR) screens and matched to those calculated by TRACE 3D by adjusting the quadrupole field. Wall-current, beam-position monitors (BPM) were used to monitor beam transport through the center of the beamline and also to measure relative beam current. The BPM performance has been reported elsewhere.[43] The BPM beam current was monitored to ensure 100% beam transmission through the wiggler tube.

The electron beam energy was measured with the first magnetic dipole using beam position monitors before and after the first bend to determine the beam centroid position. The error in electron beam energy measurements is approximately ± 2%. A high-resolution energy spectrometer at the third bend was used to measure beam energy spread and fluctuation to a precision of ± 0.025%. A typical energy spread, integrated over the 12-μs macropulse and thus including energy slew, is 0.5%. The energy fluctuation from macropulse to macropulse is ± 0.25%. The actual micropulse energy spread has not been measured, but the FWHM energy spread is calculated to be 0.25%.

5.3.2 Wiggler

For oscillation in the 4 to 10 μm region, a 24-cm untapered linear wiggler with 1-cm periods is used. Each period consists of two pairs of samarium cobalt magnets arranged with the magnetization oriented along the beam axis. The wiggler is shown in Figure 28.

The measured on-axis field was 0.42 T with a gap of 3 mm. Due to the orientation of the magnets, the third harmonic content reduces fundamental field by 0.02 T. The fundamental field is thus 0.4 T, yielding an rms wiggler parameter a_w of 0.266. Before assembly on the beamline, the wiggler was tested via the taut wire technique.[44] After the wiggler was mounted on the optical table, the area around the wiggler was found to have a constant field of approximately 4 gauss. A small correction electromagnet was used to cancel out this residual magnetic field.

5.3.3 Resonator optics

The Advanced FEL optical resonator consists of two concave mirrors mounted in vacuum with the wiggler at the center of the resonator. The 1.3836-m mirror separation and 0.70-m radius of curvature give a resonator parameter (g = 1 - L/R) of -0.9766 and Rayleigh range of 7.5 cm

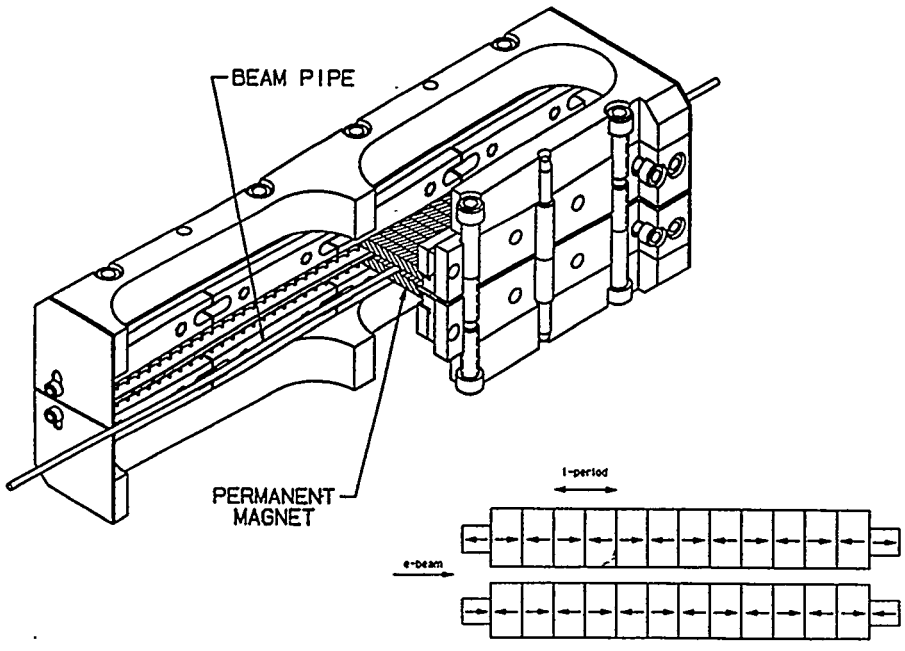

Figure 28. AFEL permanent magnet wiggler with a 1 cm period, 24 periods, and a 0.3 cm gap. The rms a_w is 0.27.

(about one-third of wiggler length). At 6 μm, the calculated lowest order mode size is 378 μm at the center of the wiggler and 753 μm at the end of the 26.3 cm-long wiggler tube. The 2.8-mm-id tube introduces an estimated loss of 0.2% for the lowest order transverse mode. However, this vignetting loss can be substantially larger if hole coupling is used because the hole forces the optical mode to have a larger diameter throughout the resonator.

Two sets of optics have been used in the Advanced FEL resonator. The first set consists of two diamond-turned gold evaporated copper mirrors. These mirrors have an averaged reflectivity of better than 99% over the mid-infrared region. However, diamond turning on concave surfaces produces grooves that scatter light and introduce an additional loss. The resonator round-trip loss with two 1% hole-coupled mirrors was measured to be ~8%. Out-coupling in metal mirrors is provided by a hole drilled in the center of the mirrors. For a hole with a radius, a, that is small compared to the empty cavity mode size, w, at the mirrors, the fraction of light out-coupled is approximately $2(a^2/w^2)$. Although metal mirrors provide broad spectral coverage, there are two problems associated with hole-coupling. First, diffraction caused by the presence of the out-coupling hole modifies the empty cavity mode in such a way that the vignetting loss at the wiggler ends increases. The vignetting loss increases as one tries to out-couple more by increasing the hole size, and so the ratio of out-coupling to total loss is relatively constant.[45] Second, alignment is difficult because the alignment HeNe beam cannot be injected through the out-coupling hole and matched into the resonator mode.

The second set of optics is ZnSe/ThF_4 multilayer dielectric (MLD) on ZnSe substrates. Two different MLD coatings with 99.5% and 99.0% reflectivity at 4.5 to 5.5 μm have been used. The transmission of each mirror, measured to be 0.5% to 1% over the 4.5 to 5.5 μm region, respectively, provides the out-coupling. Higher out-coupling is possible by tuning the FEL wavelength to either side of the coating reflectivity curve. The advantages of using dielectric mirrors are the low resonator loss (the round-trip cavity loss was almost entirely due to outcoupling). Another advantage is the ability to transmit the alignment HeNe laser beam through one of the mirrors. However, the MLD coatings are easily damaged in the forms of mm-size pits and cracks by the peak intracavity power. The coating damage limits the peak intracavity power to less than 500 MW (3 GW/cm^2 on the mirrors) and precludes sideband operation that would lead to much higher extraction efficiency.

5.3.4 FEL optical diagnostics

The FEL output was characterized with various optical diagnostics. A sensitive HgCdTe detector was used to measured the spontaneous emission, or with suitable attenuation, the coherent emission. To obtain macropulse buildup and ring-down times, a Molectron P500 pyroelectric detector with sub-nanosecond response time was used. Macropulse energy was measured, sometimes at both ends of the FEL if the outcoupling was bi-directional, with Molectron J50 and Gentec ED-200 pyroelectric energy detectors. These energy detectors are calibrated to within ± 5%. The FEL spectral characteristics were measured with an Optical Engineering spectrum analyzer. The spectrum analyzer has a 75-grooves/mm grating and a Molectron pyroelectric array at the exit focal plane.

5.3.5 FEL pulse energy

The highest macropulse energy was observed for an electron beam energy of 15 MeV and a peak current of 200 A was 240 mJ after correction for loss in transport optics. The peak beam power in each micropulse was 3 GW. The mirrors used in this experiment were a 1% hole-coupled, gold-evaporated mirror with an additional loss of 3%, and an MLD mirror that has an out-coupling of 7% at 5.8 μm. The measured ring-down is 84 ± 10 ns corresponding to a total cavity loss of 11 ± 1%. The maximum output energy recorded by the Molectron J50 energy meter was 25 mJ at the 1% out-coupling mirror of the resonator through a CaF_2 window. The Gentec ED-200 energy meter recorded 175 mJ through an uncoated CaF_2 window, two Cu mirrors, and an uncoated CaF_2 lens. The total output energy after correcting for reflection loss was 240 mJ. Ignoring the ends of the macropulse, there are approximately 1200 micropulses in the 11-μs saturated portion of the macropulse. The energy in each micropulse was thus 200 μJ. The estimated peak optical power was 20 MW corresponding to an efficiency of converting electron beam power into light of 0.7%. The intracavity extraction efficiency is estimated to be 1%, one-half of the theoretical limit without sideband of 2% (1/2N). A sample 8-μs long macropulse is shown in Figure 29.

5.4 Schedule

The AFEL was a five year program funded with Los Alamos institutional funds. Table 2 is a list of the accelerator and beamline commissioning activities. Table 3 is a list of the free-electron laser commissioning activities.

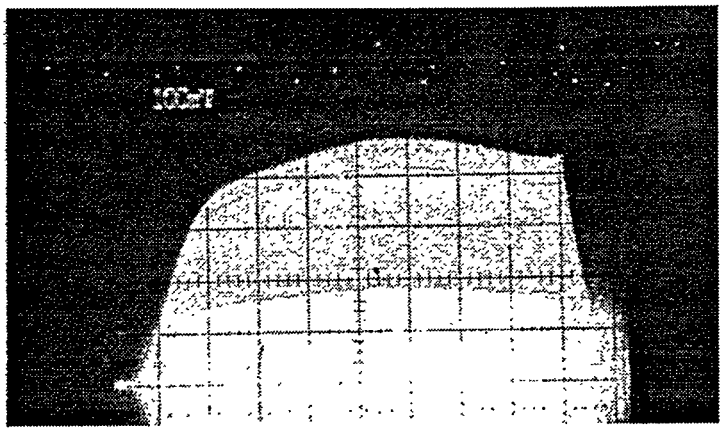

Figure 29. The AFEL optical output. The horizontal divisions are 1 μs/div and the vertical scale is output power in relative units.

Table 2. A history of AFEL accelerator commissioning activities

Mar 1990 - Jan 1991	Simulations
Jan 1991 - Jan 1992	Design and Off-site Fabrication
Jan 1992 - March 1992	Linac Commissioning
July 1992	First Electron Beam
Sep 1992 - Nov 1992	Beam to Spectrometer
January 1993	100% Beam Transport

Table 3. A history of the AFEL laser commissioning activities

February 1993	Spontaneous Emission at 5.2 mm (~0.1 mW)
April 1993	Lasing at 4.7 mm (7 mW)
October 1993	34 mW
December 1993	1.6 Watts

5.5 Experimental Results

Emittance measurements in a photoinjector are complicated by one of the photoinjector's advantages. Because of the rapid acceleration and lack of other beamline components in the gun region, the longitudinal phase space of the beam does not thermalize. As a result of the non-thermalization, different longitudinal parts of the beam propagate with their own trajectories. This complicates the analysis of the beam's phase space ellipse. Commonly used techniques for measuring emittance, such as

pepperpot technique or quadrupole scans, can lead to erroneous phase-space emittance measurements.

As described in Section 4.1.2, the first photoinjector experiment used a pepperpot to measure the emittance. Because of the longitudinal variations in phase-space, the emittance was underestimated by a factor of four. In this section, I will describe difficulties in using a quadrupole scan technique to determine the beam's emittance.

For a thin lens, the rms unnormalized emittance, ε_{un} can be calculated by fitting the beam spot size x_s to the coefficients of $1/f$ in the following

$$x_s^2 = x_{\min}^2\left[1+\{L^2\varepsilon_{un}(1-f_w/f)/(x_{\min}^2 f_w)\}^2\right], \tag{5.1}$$

where ε_{un} is the unnormalized rms emittance, L is the spacing between the quadrupole and image screen, f is the focal length of the quadrupole, f_w is the focal length that gives the minimum spot size x_{min}.[46] The focal length of a quadrupole is $\beta\gamma m_e c/(leB)$, where β, γ are the relativistic factors, m_e is the mass of an electron, c is the speed of light, l is the quadrupole length, e is the electron charge, and B is the quadrupole field gradient.

For a thick or thin lens, the spot size x_s can be fit using the Twiss parameters[47] with the following formula,

$$x_s^2 = \varepsilon_{un}\left[m_{12}^2\gamma_q - 2m_{11}m_{12}\alpha_q + m_{11}^2\beta_q\right], \tag{5.2}$$

where γ_q, β_q, and α_q are the Twiss parameters of the beam at the quadrupole. The coefficients of the Twiss parameters are from the Twiss parameter transfer matrix for a thick lens,

$$\begin{aligned} m_{11} &= \cos(\theta) - d\theta\sin(\theta)/L \\ m_{12} &= d\cos(\theta) + L\sin(\theta)/\theta \\ \theta &= L\sqrt{eB/(\beta\gamma mc)} \end{aligned} \tag{5.3}$$

where d is the quadrupole's axial length and L is the spacing from the end of the quadrupole to the image screen. Using the identity $\beta_q\gamma_q-\alpha_q^2=1$, the rms unnormalized emittance can be calculated from the coefficients of the fit.

The experimental data and the fit using the Twiss parameters are shown in Figure 30. The thin lens fitting procedure was also used on the experimental data. The data and the fit were within 10%. The rms emittance as calculated from the fit for either the data spot sizes or for the PARMELA spot sizes is 2.3 π mm-mrad. However, the PARMELA simulation gives an integrated rms emittance of 5.3 π mm-mrad.

The discrepancy in emittance is due to the manner in which the data is analyzed. Measuring the full distribution of an image on a screen is susceptible to many errors. In particular, the correction of data due to baseline shifts and the non-linear response of cameras, especially at low intensity, is very difficult. Unfortunately, the rms emittance numbers are very sensitive to the tails of the distribution. So instead, many researchers measure an unambiguous parameter of the spot-size, the full-width half-maximum. As can be seen in Figure 30, the agreement between the FWHM's from the experimental measurement and the FWHM's from PARMELA is very good. However, because of the longitudinal dynamics of different slices, the FWHM measurement cannot be used to directly compute the beam's emittance. In Figure 30, the dashed curve shows the FWHM as calculated from the rms spot sizes from PARMELA. By using FWHM of spot calculated from the rms emittance, the quadrupole scan fit gives an emittance close to the calculated emittance.

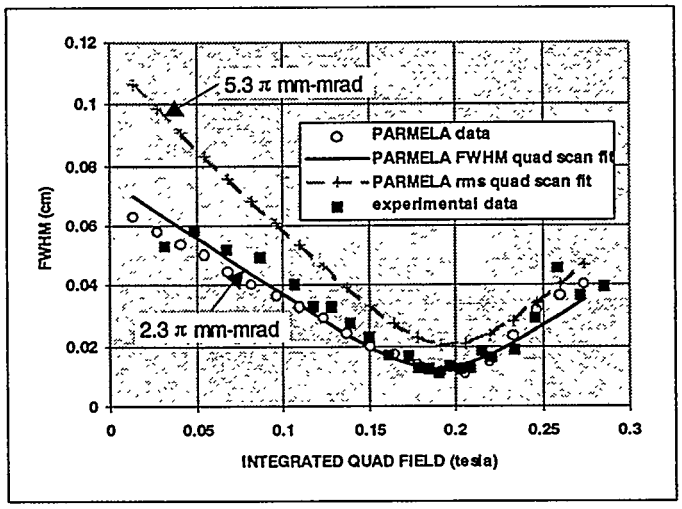

Figure 30. The data and PARMELA simulation are for a quadrupole scan with the FWHM taken at a screen 30 cm downstream from the quadrupole. The electron pulse is 1.9 nC at 17.2 MeV. The beam is produced by a Cs_2Te cathode illuminated by a 8 ps laser pulse. The laser's spatial profile is a 6 mm FWHM Gaussian clipped with a circle of 5.2 mm diameter. The FWHM of each slice at the screen is plotted as a function of the quadrupole gradient.

The variation of FWHMs at the screen of the individual slices with changing quadrupole strength is shown in Figure 31. The reason for the discrepancy in emittance is readily apparent. The ends of the micropulse are focused differently than the middle of the pulse. The FWHM spot size measurement is thus complicated by the different longitudinal portions of the pulse contributing to the FWHM in differing amounts as the quadrupole is varied.

The minimum spot size is dependent on the cathode temperature and any residual magnetic field on the cathode. Thus far, the cathode temperature of Cs_2Te has not been measured. The cathode initial emittance can be inferred by adding a minimum spot size to the PARMELA spot sizes (square root of sum of squares). From the experimental data, this gives an initial emittance of 2.8 π mm-mrad, corresponding to a transverse energy of 1.2 eV. The partition of this energy between residual magnetic field at the surface of the cathode and cathode temperature could not be determined.

Finally, the large solenoid around the cathode region is the main steering and focusing element in the system. This results in the beam's Twiss parameters, as well as the beam's propagation direction, being very sensitive to the magnitude and tilt of the solenoid's field. For the case shown above, the measured value of the large solenoid's field was within 1% (experimental error was +/-2%) of the value predicted by PARMELA.

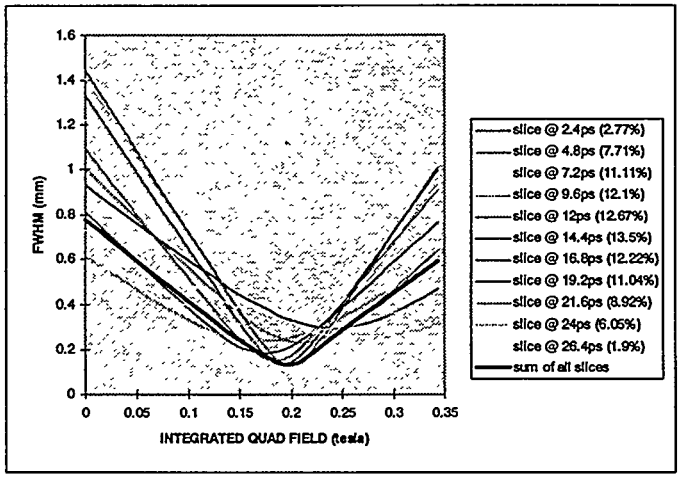

Figure 31. The TAPE2 PARMELA output was processed by dividing the longitudinal length of the pulse into 11 equal segments. The FWHM of each slice at the screen is then plotted as a function of the quadrupole gradient. The fraction of charge in each slice is shown in the legend. The thick black line is the summation of all the individual FWHM's. To make sure the slicing was done properly, the summation is compared with the normal output of PARMELA (an integration over all slices).

Changes in magnetic field as small as 1% are easily observable in simulation and have a significant effect on the beam's Twiss parameters.

6. APPLICATIONS

The two classes of applications emerge as the most likely for FELs are research and commercial applications. The application of FELs for research depends on whether an existing facility is used or a new facility is being built. If the FEL is added to an existing accelerator facility then the operations staff can be a sub-group of the existing operations staff. This significantly reduces costs since experts in subsystems are already present (such as controls and rf systems). Also, an FEL added to an existing facility is typically a small fraction of the overall facility cost, the FEL can use leftover and modified existing components, and the utilities are largely covered.

If a new FEL is being built for research activities, then the design of the FEL must be low-cost and have a design that does not require a large crew of experts. However, sophisticated operators are in good supply, such as post-doctoral students.

Finally, commercial applications have the most restrictive set of requirements. The FEL must be low-cost, have low-maintenance, and have a low-operating cost. The FEL must also be user-friendly, i.e., employ one non-specialist operator. These requirements imply a high level (cost) of advanced engineering.

The next sections are a very brief summary of the National Academy of Science report on the applications of FELs. For more detailed information please refer to the National Research Council's report.[48] The report summary is divided into four sections based on wavelength: 1000 to 10 microns, 10 microns to 200 nm, 200 nm to 10 nm and x-ray wavelengths.

6.1 1000 to 10 microns

The 1000 to 10 micron wavelength band offers many opportunities for an intense, tunable light source for studies in surface science, chemistry, solid state physics, biophysics, and plasma physics. The following list indicates some potential applications not address by presently available sources.

Some surface science applications are the measurement of energy distributions and line shapes of intramoleculer vibrations, of the chemisorption of surfaces, and of the adsorption of species during

chemical reactions. A chemistry application is the study of energy transfer in molecules in the gas and liquid phase. Some solid-state physics applications are: the measurement of phonon, plasmon, magnon, and inter-sub-band transition excitations in condensed matter, the direct probing of defect modes and buried interfaces, the probing of mode-mode interactions, and the driving of preselected strongly non-equilibrium states and studying their relaxation. A biophysics application is measurement of low-frequency modes of large biomolecules such as nucleic acids and proteins. Some plasma physics applications are plasma heating with tens of megawatts, plasma diagnostics, measuring phase shift of waves sent through a plasma, and measuring reflections of waves from critical density regions. A final application is isotope separation.

6.2 10 microns to 200 nm

In the 200 nm to 10 micron band, conventional lasers give stiff competition to free-electron lasers. The biggest problem is the cost comparison between FELs and conventional laser systems, with conventional systems costing between $5K to $250K.

An FEL's real advantage in this wavelength band is high-power at wavelengths not accessible to high-power conventional lasers. For instance, the batteries in satellites determine the satellite's operating lifetime. Power-beaming at 0.85 microns, the peak of the photocell response, would increase the satellite's lifetime several years. Another application for an FEL is in atmospheric science. Atmospheric modeling requires knowledge about the concentration of water and wind patterns between 20 km and 100 km. The conventional technique is to launch balloons. A high-power tunable laser could be used to sweep over waters rotational lines and get temperature information as well as concentration and wind speed as a function of altitude. Finally, a reliable, robust high-power laser would have defensive military applications.

6.3 200 nm to 10 nm

In the 10 nm to 200 nm band other sources are available by using 4-wave mixing of lasers or synchrotrons. Some possible FEL applications are: to study photodissociation dynamics by pumping molecules with the FEL and studying fragments with a tunable probe laser; to do photoelectron spectroscopy by probing many molecules (like radical and weakly bound complexes) not accessible now; to do pump-probe photoemission to study long-lived excited states in semiconductors for information on intrinsic and defect states; and for the commercial processing of polymers.

6.4 X-ray Wavelengths

In the 0.1 to 10 nm wavelength, the light sources do not have the peak power or coherence of an FEL. Competing light sources are synchrotrons, laser targets, Compton backscattering. One application using time-correlation spectroscopy is measuring the time dependence of speckle patterns. This type of spectroscopy gives information about motion on less than 100 nm scales. A set of applications exists in the X-ray spectroscopy, such as: magnetic scattering at absorption edges to study magnetically ordered systems, inelastic x-ray scattering to probe high-energy phonons and magnons, and dynamical behavior of quasi-crystalline and fluid-phase short-range order. Another application is the microscopy and holography of biological process in cells.

Although not an FEL based system, Compton Back-Scattering (CBS) can be used as an efficient source tunable x-rays from a bright electron beam accelerator. The properties of a CBS system are angular dependent bandwidth and low electron beam energy (less than 25 MeV). If the accelerator is photoinjector-based, the time correlation of scattering laser and electrons is automatic. If the accelerator is part of a compact, low-cost system then two medical applications look promising: mammography and coronary angiography. These medical applications are interesting because a narrow x-ray linewidth tuned to the 33 KeV edge of iodine would give better definition and at a greatly reduced dose.

The following is an example CBS system based on using the AFEL accelerator and assuming an electron beam energy of 22 MeV and a quadrupled Nd:YLF (4.6 eV) laser. The scattering of the 4.6 eV photons off the electron beam gives x-rays at the 33-KeV edge of iodine. The x-ray photon energy, $E_{x\text{-}ray}$, is calculated by

$$E_{x\text{-}ray} = 4*E_{laser}*E^2_{electron}/(mc^2)^2, \qquad (6.1)$$

where E_{laser} is the photon energy, $E_{electron}$ is the electron energy, m is the electron mass, and c is the speed of light. The x-ray flux is

$$flux = N_e*N_{laser}*\sigma/A, \qquad (6.2)$$

where N_e is the number of electrons, N_{laser} is the number of laser photons, σ is the cross-section, and A is the interaction area. Assuming a cross-section of 6.65×10^{-24} cm^2 and a 5% bandwidth corresponds to +/- 5 mrad, then each 20-ps electron micropulse gives 1000 x-ray pulses. Each 30

microsecond macropulse has 3000 pulses, and the maximum repetition rate is 60 Hz giving a total of 1.8×10^8 photons/second.

6.5 Commercial Applications

There are many commercial applications of electron beams, however, almost all do not require high brightness electron beams. A sample list is: sterilization of medical products, food containers and products, sewage; decomposition/precipitation of chemical pollutants and hazardous materials; cancer therapy; cross-linking of polymers in insulation for wires and cables and polymerization; curing of composites, surface coatings, magnetic recording media, and adhesives; radiography; materials modification for ion implantation, gemstones, and radiation hardening.

6.6 High-Energy Physics

For high-energy physics the applications are reducing the acceptance requirements of a damping ring, and thereby reducing the cost, or possibly eliminating a damping ring completely. Of course, a ring would still be needed for the positrons. Another interesting application requiring both a high-brightness electron beam and an FEL is a gamma-gamma collider.[49]

7. SUMMARY

Photoinjector technology has had significant developments in the decade since its inception. Designs now span a large range in accelerator frequencies and electron pulse requirements. The photocathode source, though difficult, is not a major impediment to implementing a photoinjector-based system. However, the amplitude stability of the drive laser for the photocathode is an issue.

Design of a 20-MeV compact linac based on the photoinjector has been completed. The linac is approximately 1.2 m long and is operated with a 15-μs macropulse at up to 15 Hz with a 0.5-A average during the macropulse. The design of the linac is based on emittance reduction by reversing the effects of space charge after the photoinjector gun. An exact comparison with simulation is required for a thorough understanding of the phase space of the pulse. For a good simulation, an accurate measurement of magnetic fields, photocathode laser profile, accelerating fields, and phasing of the laser and rf is required. With accurate measurements, good agreement between the experiment and PARMELA simulations can be obtained.

The production of high-current high-brightness electron beams has enjoyed considerable progress over the last several years, mainly because of changes in the requirements imposed by free electron lasers. Several approaches show considerable potential for producing very bright electron beams. The concept of placing a photoemissive source in an accelerating structure has been demonstrated. The basic physics of photoinjectors is understood. Several groups around the world are designing bright beams based on this technology and continued improvement in photoinjector design is expected.

ACKNOWLEDGEMENTS

The author thanks John Fraser with whom the initial work on the photoinjector program was accomplished. Also, I thank Dominic Chan, Dinh Nguyen, John Kinross-Wright, Karl Meier, Lloyd Young, Rick Wood, Ed Gray, Tai-Sen Wang, Robert Springer, Bruce Lambertine, Valerie Loebs, Joel Johnson, Peter Oettinger, Bill Herrmannsfeldt, Roger Miller, Harold Hanerfeld, Bill Wilson, Bob Austin, Carl Timmer, Boyd Sherwood, Louis Rivera, John Plato, Mike Weber, Floyd Sigler, Steve Gierman, Steve Kong, Steve Russell, Steve Hartmann, Alessandra Lombardi, Dodge Warren, Cliff Fortgang, Bob Kraus, Doug Gilpatrick, and John Ledford for their contributions to the photoinjector projects. The author acknowledges Bruce Carlsten, Bill Herrmannsfeldt, Roger Miller, Charles Sinclair, Todd Smith, Steve Benson, Ken Batchelor, S. Chattopadhyay, and R. Dei-Cas for their helpful discussions and for information on bright electron sources. The author is indebted to many individuals for information on their projects. In particular, I wish to thank Chris Travier, Steve Kong, John Adamski, Shien-Chi Chen, Harold Kirk, Claudio Pellegrini, and Jim Simpson. Also Jerry Watson and Stanley Schriber are acknowledged for their continued support.

REFERENCES

1. C. LeJeune and F. Aubert, *Applied Charged Particle Optics*, A. Septier, Ed., Advances in Electronics and Electron Physics, Supp. 13A, 159-259 (1980)
2. K. L. Brown, *Nucl. Inst. And Meth.* **187**, 51-65 (1981)
3. J. D. Lawson, *The Physics of Charged Particle Beams*, (Oxford Univ. Press, 1978) 175
4. J. D. Lawson, *ibid.*, 199
5. W. D. Herrmannsfeldt, *Physics of Particle Accelerators*, AIP Conf Proc. 184, 2, 1533-1542 (1988)
6. J. R. Pierce, *Theory and Design of Electron Beams*, (van Nostrand, 1949)

7. T. I. Smith, *1986 Linear Conf. Proc.*, SLAC-303, 421-425 (1986)
8. T. Energa, L. Durieu, D. Michelson, and R. Worsham, *IEEE Trans. Nucl. Sci.* **32** (5), 2936 (1985)
9. S. V. Benson, J. Schultz, B. A. Hooper, R. Crane, and J. M. J. Madey, *Nucl. Instr. and Meth.*, **A272**, 22-28 (1988)
10. P. E. Oettinger and I. Bursuc, *IEEE Part. Accel. Conf,* IEEE cat. no. 87CH2387-9, **1**, 286 (1987)
11. J. Fischer, T. Srinivasan-Rao, and T. Tsang, *Sources '94*, Schwerin, Germany, Sept. 29 - Oct.4, 287-289 (1993)
12. G. Suberlucq, *Sources '94*, Schwerin, Germany, Sept. 29 - Oct.4, 557-561 (1993)
13. C. Travier, *6th Workshop on Advanced Accel. Concepts, Lake Geneva, WI, June 12-18,* (1994)
14. Private communication from M. E. Conde, UCLA/ANL (1994)
15. Private communication from C. Pellegrini, UCLA (1994)
16. D. J. Bamford, M. H. Bakshi, and K. A. G. Deacon, *Nucl. Inst. And Methods*, **A318**, 377-380 (1992)
17. Y. Tur, *Sources '94*, Schwerin, Germany, Sept. 29 - Oct.4, 572-576 (1993)
18. E.Chevallay, J. Durand, S. Hutchins, G. Suberlucq and M. Wurgel, *Nucl. Instr. and Meth.* **A340**, 146 (1994)
19. S. H. Kong, J. Kinross-Wright, D. C. Nguyen, and R. L Sheffield, *J. Appl. Phys.*, **77**, 1-8 (1995)
20. M. Yoshioka, *Sources '94*, Schwerin, Germany, Sept. 29 - Oct.4, 624-629 (1993)
21. J. S. Fraser, R. L. Sheffield, and E. R. Gray, *Laser Acceleration of Particles AIP Conf. Proc.*, no. 130, 598, (1985); J. S. Fraser, R. L. Sheffield, and E. R. Gray, *Nucl. Inst. And Methods*, **250**, 71-76 (1986)
22. B. E. Carlsten, *Nucl. Inst. And Methods*, **A285**, 313-319 (1988)
23. J. S. Fraser and R. L. Sheffield, *IEEE J. Quant. Elec.*, **QE-23**, 1489-1496 (1987)
24. W. Herrmannsfeldt, R. Miller, and H. Hanerfeld, SLAC-PUB-4663, (1988)
25. E. R. Gray and J. S. Fraser, *Proc. 1988 Linear Accel. Conf.*, Williamsburg, VA, October 3-7, CEBAF Report 89-001, 338-340 (1988)
26. S. V. Benson, J. M. J. Madey, E. B. Szarmes, A. Bhowmik, J. Brown, P. Metty and M. S. Curtin, *Nucl. Instr. and Methods*, **A296**, 762 (1990)
27. J. Early, J. Barton, G. Busch, R. Wenzel, and D. Remelius, *Nucl. Instr. and Meth.*, **A318**, 381-388 (1992)
28. R. L. Sheffield, R. H. Austin, K. D. C. Chan, S. M. Gierman, J. M. Kinross-Wright, S. H. Kong, D. C. Nguyen, S. J. Russell, and C. A. Timmer, *Proc. 1993 Part. Accel. Conf.*, **4**, 2970-2972 (1993)
29. D. H. Dowell, K. J. Davis, K. D. Fridell, E. L. Tyson, C. A. Lancaster, L. Milliman, R. E. Rodenburg, T. Aas, M. Bemes, S. Z. Bethel, P. E. Johnson, K. Murphy, C. Whelen, G. E. Busch, and K. K. Remelius, *Appl. Phys. Lett.*, **63**, no. 15, 2035-2037 (1993)
30. S. Joly et al., *Proc. 1990 European Part. Accel. Conf.*, 140-142 (1990)
31. K. Batchelor, I. Ben-Zvi, R. C. Fernow, J. Fischer, A. S. Fisher, J. Gallardo, G. Ingold, H. G. Kirk, K. P. Leung, R. Malone, I. Pogorelsky, T. Srinivasan-Rao, J. Rogers, T. Tsang, J. Sheehan, S. Ulc, M. Wookle, J. Xie, R. S. Zhang, L. Y. Lin, K.

T. McDonald, D. P. Russell, C. M. Hung, and X. J. Wang, *Nucl. Inst. and Methods*, **318**, 372-376 (1992)

32. S. C. Chen, J. Gonichon, L. C-L. Lin, R. J. Temkin, S. Trotz, B. G. Danly, and J. S. Wurtele, *Proc. 1993 Par. Accel. Conf.*, 4, 2575-2577 (1993)
33. P. Schoessow, E. Chojnacki, G. Cox, W. Gai, C. Ho, R. Konecny, J. Power, M. Rosing, J Simpson, N. Barov, and M. Conde, IEEE Proc. of Part. Accel. Conf., May 1-5, Dallas, Tx, (1995)
34. H. Kirk, *Sources '94*, Schwerin, Germany, Sept. 29 - Oct.4, 392-398 (1993)
35. B. E. Carlsten, Porc.10th Int. FEL Conf., Jerusalem, Israel, 1988, *Nucl. Instr. and Meth.*, **A285**, 313 (1989); B. E. Carlsten and R. L. Sheffield, *Proc. 1988 Linac Conf.*, Williamsburg, Va, 1988, CEBAF Report 89-001, 365-369 (1989); B. E. Carlsten, *Proc. 1989 IEEE Part. Accel. Conf.*, Chicago, IL, IEEE Catalog no. 89CH2669-0 313 (1989); B. E. Carlsten, *Part. Accel.*, **49**, 27-65 (1995)
36. B. E. Carlsten, *Part. Accel.*, **49**, 34-37 (1995)
37. K. C. D. Chan, R. H. Kraus, J. Ledford, K. L. Meier, R. E. Meyer, D. Nguyen, R. L. Sheffield, F. L. Sigler, L. M. Young, T. S. Wang, W. L. Wilson, and R. L. Wood, *Nucl. Instr. and Methods*, **A318**, 148-152 (1992)
38. P. G. O'Shea, S. C. Bender, S. A. Byrd, B. E. Carlsten, J. W. Early, D. W. Feldman, R. B. Feldman, W. J. D. Johnson, A. H. Lumpkin, M. J. Schmitt, R. W. Springer, W. E. Stein and T. J. Zaugg, *Nucl. Instr. and Methods*, **A318**, 52-57 (1992)
39. T. F. Wang, K. C. D. Chan, R. L. Sheffield, and W. L. Wilson *Nucl. Instr. and Methods*, **A318**, 314-318 (1992)
40. W. B. Colson, G. Dattoli, and F. Ciocci, *Phys Rev. A*, **64**, 2 (1985)
41. S. Hartmann, A. Lombardi, R. L. Sheffield, and T. Wang, *Nucl. Instr. and Methods*, **A318**, 319-322 (1992)
42. D. C. Nguyen, R. H. Austin, K. C. D. Chan, C. Fortgang, W. J. D. Johnson, J. Goldstein, S. M. Gierman, J. Kinross-Wright, S. H. Kong, K. L. Meier, J. G. Plato, S. J. Russell, R. L. Sheffield, B. A. Sherwood, C. A. Timmer, R. W. Warren, and M. E. Weber, *Nucl. Instr. and Meth.*, **A341**, 29-33 (1994)
43. K. C. D. Chan, K. L. Meier, D. C. Nguyen, R. L. Sheffield, T. S. Wang, R. W. Warren, W. Wilson and L. M. Young, *1992 Linear Accelerator Conf. Proc.*, Ottawa, Ontario, Canada, AECL-10728, **1**, 37-39 (1992)
44. J. D. Gilpatrick et al., *IEEE Proc. of Particle Accelerator Conf.*, (1993)
45. D. W. Preston and R. W. Warren, *Nucl. Instr. and Methods*, **A318**, 794-797 (1992)
46. M. Xie and K. J. Kim, *Nucl. Instr. and Meth.*, **A318**, 877-884 (1992)
47. B. E. Carlsten, J. C. Goldstein, P. G. O'Shea, and E. J. Pitcher, *Nucl. Inst. And Methods*, **A331**, 791-796 (1993)
48. S. Humphries, Jr., "Charged Particle Beams," *John Wiley and Sons, Inc.*, 143 (1990)
49. National Reasearch Council, "Free-Electron Lasers and Other Advanced Sources of Light," Board on Chemical Sciences and Technolgoy, National Reasearch Council, 2101 Constitution Ave. N.W., Washington, D.C., 20418 (1994)
50. A. M. Sessler, "Photon-Photon Colliders," 1995 PAC conference, Dallas, TX, May 1-5 (1995)